Space: Science & Technology
A SCIENCE PARTNER JOURNAL

RESEARCH ARTICLE

Design and Realization of Landing–Moving Integrated Gear for Mobile Lunar Lander

Xianghua Zhou[1†], Cong Niu[2†], Shan Jia[1,3,4*], Jinbao Chen[1,3,4], Vyacheslav Mikhailovich Devaev[5], and Jinhua Zhou[6]

[1]Academy of Astronautics, Nanjing University of Aeronautics and Astronautics, Nanjing 211106, China. [2]University of Strathclyde, Glasgow G1 1XQ, UK. [3]Laboratory of Aerospace Entry, Descent and Landing Technology, Nanjing 211106, China. [4]Key Laboratory of Detection Mechanism Technology for Deep-Space Planet Surface (Nanjing University of Aeronautics and Astronautics), Ministry of Industry and Information Technology, Nanjing 211106, China. [5]Kazan National Research Technical University named after A.N. Tupolev-KAI, Kazan 420111, Russia. [6]School of Mechanical Engineering, Shandong University, Jinan 250061, China.

*Address correspondence to: jiashanazz@nuaa.edu.cn
†These authors contributed equally to this work.

Citation: Zhou X, Niu C, Jia S, Chen J, Devaev VM, Zhou J. Design and Realization of Landing–Moving Integrated Gear for Mobile Lunar Lander. *Space Sci. Technol.* 2024;4:Article 0169. https://doi.org/10.34133/space.0169

Submitted 25 October 2022
Accepted 3 April 2024
Published 5 August 2024

For the needs of manned landing, station construction, and material transfer in future lunar exploration missions, the paper proposes a landing–moving integrated gear (LMIG) for mobile lunar lander (MLL), establishes and optimizes the models of cushioning energy-absorbing and movement planning, respectively, and conducts the prototype tests. First, the design requirements of LMIG are given, and the system composition of LMIG and the configuration design of each subsystem are introduced. Second, the effective energy-absorbing model of the aluminum honeycomb is established and experimentally verified, a three-stage aluminum honeycomb buffer is designed and experimentally verified, and the buffer mechanism of LMIG is verified by simulations under various landing conditions. Furthermore, the kinematic and dynamic models of LMIG are established, the moving gait is designed by the center of gravity trajectory planning method, and the driving trajectory during the stepping process is optimized with the goal of minimal jerk of motion. Finally, a cushioning test prototype and a walking test scaled prototype of LMIG are developed, and single leg drop test and ground walking test are carried out. The results show that the established model of LMIG is reasonable, the designed buffer and gait of LMIG are effective, the developed prototypes of LMIG have good cushioning and movement performance, the LMIG's maximum value of overload acceleration is 6.5*g*, and the moving speed is 108 m/h, which meets the design requirements.

Introduction

In lunar exploration missions, landing and roving has been an important component due to their advantages of direct exploration, such as drilling, sampling, and roving, compared to fly-by, fly-around, impact, and other exploration methods. This combined approach has proven its effectiveness in many projects, the lander is used to absorb the impact energy of the landing process, and the rover is used to carry out mobile probing after landing. Typical cases have achieved remarkable achievements: Soviet Union Luna Project [1], American Apollo Project [2], and China Chang'e Project [3] have all realized lunar sampling and roving exploration. However, the combined approach of lander and rover shows certain limitations with the increase of the number and complexity of lunar exploration missions.

1. The cushioning capacity is limited. The traditional landing gear does not have the active cushioning capacity, so it is impossible to ensure that each landing leg starts working at the same time and this leads to redundancy in design. In addition, the tilted posture of the lander after landing has an adverse impact on subsequent operations.

2. The detection range is limited. Although the rover can expand the detection range, due to the constraints of volume, energy, communication, and detection route, its detection range is still limited to the restricted area around the lander. Meanwhile, the wheeled rover has poor terrain passing capacity, which makes it difficult to cross complex terrain such as gravel, hill, and gully.

3. The scientific gains are limited. The landing site of the lander is mostly selected from flat terrain due to the limitation of landing capacity. However, the rugged terrain is rich in volcanic ejecta, bedrock outcrops, and things like that, which will be the focus of future exploration. Therefore, this approach to a great extent limits the scientific gains of the missions.

4. It has poor usability for manned exploration and construction of lunar station. In order to ensure the safety of lunar station, a suitable safety distance is usually set between the

landing site and the station. The traditional approach does not have the ability to move and thus cannot undertake the task of goods and materials transfer, passenger transport, lunar surface operations, station construction through the combination of multiple landers, etc.

In view of these limitations, many scholars proposed to design a mobile lander to solve these problems. The relevant research can be seen in researches by Benton [4,5], Kennedy [6], Huang and Howe [7], Mankins [8], Wilcox [9], Zhang et al. [10], and Jia et al. [11,12]. Although there is much research on the mobile lander, most of the research contents are assumptions or only focus on a single aspect such as mechanism design and optimization [13,14]. In order to comprehensively consider the function realization of the mobile lander, the authors study various aspects of mobile lunar lander (MLL) and present a novel and practical design architecture for the landing–moving integrated gear (LMIG) of the MLL with a reliable cushion–actuation–transmission functions. The LMIG, constituted by load-bearing mechanism, cushion mechanism, drive mechanism, transmission mechanism, and control system, can help MLL realize cushioning and moving functions. But at the same time, this complex mechanism poses a tough challenge on the design issue under the demands of comprehensive performances in landing and driving. Therefore, three aspects need to be considered.

The first is the realization of landing function. The cushioning function is the key to realize soft landing detection on the lunar surface, and is usually realized by landing gear because of its simple structure and high reliability. The famous lunar exploration missions both adopted landing gear based on aluminum honeycomb: Apollo 11 Project [15] realized the first manned landing on the lunar surface; Luna 16 Project [16] realized the first automatic lunar sampling and return; Chang'e 4 Project [17] realized the first lunar far side landing and exploration. For this reason, landing gear based on aluminum honeycomb has been studied widely. The mathematical modeling methods [18], numerical methods [19,20], simulation methods [21], and experimental methods [22,23] are generally used to test the mechanical properties of the aluminum honeycomb materials. After much experimental studies, it was found that thickness [24], edge length [25,26], and impact velocity [27] have substantial effects on the cushioning performance of the aluminum honeycomb material. Furthermore, in order to analyze the cushioning performance of aluminum honeycomb more quickly, the finite element method and multi-body system dynamics method have been used for the analysis [21,28]. In the study of landing dynamics, scholars use dynamic simulation and experimental analysis methods and find that landing posture, landing slope, and lunar soil physical property parameters have an impact on landing stability [29,30]. From the previous research, it can be concluded that aluminum honeycomb cushioning performance depends on its geometric parameters and landing stability depends on its landing conditions. In this paper, the authors present an effective and fast design method for the landing gear of the MLL, using theoretical derivation, simulation analysis, and experimental verification. This method will promote the development of cushioning technology for the MLL.

The second is the realization of movement function. The movement function is a prerequisite for the realization of a series of tasks in the lunar surface. Due to the lack of successful cases about MLL, the research results of legged robots can be used for reference. In general, the realization of movement function is constituted by actuation–transmission mechanism design, movement trajectory planning, and gait planning. Han et al. [31] and Yin et al. [32] both adopted the method of adding an actuation–transmission mechanism to the landing leg to realize the movement function of the lander. The difference is that Han et al. used an additional linkage mechanism to drive the landing legs and relies on the landing gear to achieve the cushioning function, while Yin et al. installed an integrated drive unit at the revolute joint of the landing legs, which has both cushioning and driving functions. Trajectory planning generally uses conic curves [33], spline curves [34], combined curves [35], and other curves to plan the trajectories of foot-end and drive-joint, and it can be optimized with the conditions of minimum jerk, energy, or time [36,37]. The purpose of gait planning is to realize stable moving of the lander in rough terrain. In the field of legged robots, gait planning has been studied fully and divided into static gait and dynamic gait according to the different proportion of the touchdown time of a single leg in the gait cycle time [38]. Considering that the mobile lander needs to undertake tasks such as transportation of large mass loads, it is difficult to use dynamic gait, and therefore, the static gait is selected for gait planning. Further, scholars studied gait generation methods and developed center of gravity (COG) [39], zero moment point (ZMP) [40], central pattern generator (CPG) [41], and other methods. In view of the previous research, the authors present an LMIG and design its drive-joint trajectory and movement gait.

The last is the ground test of the prototype. Sufficient ground test plays an important role in ensuring the success of mission. According to the functional requirements of MLL, its ground test can be divided into two parts: cushioning performance test and movement performance test. Qi et al. [42] proposed a cushioning performance test method for the full-scale lander under the Earth's gravity field and verified the cushioning performance under different landing conditions. Yang et al. [43] conducted a single leg cushioning test of the lander and obtained the force between the landing gear and the body of lander, the force between the landing gear and the ground, and the impact acceleration during the process of the landing. Zhu and Jin [44] designed a leg-compliant control platform system and tested the stability of the robotic control algorithm, and the result shows that the algorithm can ensure the moving stability of the robot. In order to test the cushioning and movement performance of LMIG, the ground tests of LMIG have been designed and carried out.

In summary, to meet the soft landing and moving requirements of MLL for the future lunar exploration missions, this paper proposes an LMIG for MLL and carries out mechanism design, model building, simulation analysis, and experimental verification around the implementation of its cushioning and movement function. In addition, this paper can provide a reference for the design of MLL in the future.

Requirements and Constraints of LMIG

Main tasks and functional requirements

The functional requirements for LMIG are listed below. The main tasks include landing, ascent, transportation, lunar station construction, and others.

1. Own the capability of soft landing on the lunar surface
2. Adjust the attitude of lander according to the launch requirement of the ascent stage

3. Own the ability to move and patrol on the lunar surface
4. Complete the transportation of goods and materials, equipment, passengers, etc.
5. Make multiple landers dock autonomously or manually to form a lunar surface station

Performance constraints

Based on the above tasks and functional requirements, the weight, envelope dimension, cushioning performance, and movement performance of LMIG are constrained in Table 1.

Configurations Design of LMIG

Compositions and working procedure of LMIG

Based on the mission requirements of the MLL, the LMIG needs to achieve fold landing leg, unfold landing leg, landing, attitude adjustment, lunar surface movement, and other actions. Therefore, the LMIG is a complex system with many components. It can be further divided into three subsystems: deformation mechanism, cushioning-driving integrated landing leg, and movement control system. Among them, the deformation mechanism is used to change the orientation and state of the landing leg. It is composed of fold–unfold mechanism and configuration–transfer mechanism. The former is used to ensure that the landing leg is folded before launch and unfolded before landing, and the latter makes the landing leg change to a beneficial orientation for movement after landing. The cushioning-driving integrated landing leg is used to absorb impact energy during landing and move on the lunar surface after landing, which is composed of landing legs and energy-absorbing driving integrated buffers. The legs can bear the weight of the body of lander, and the buffers can realize cushioning and driving functions. The movement control system is used to calculate the movement value of landing legs according to the gait planning algorithm and accurately control the LMIG to move steadily, which is mainly composed of gait generator and movement controller. The system composition of LMIG is shown in Fig. 1.

The working procedure of LMIG for the MLL is shown in Fig. 2. The procedure mainly includes the following:

Table 1. The specifications of LMIG for mobile lunar lander

Items	Specifications
Folded size (mm)	5,400 × 5,400[a]
Unfolded size (mm)	4,000 × 4,000[a]
Load capacity (kg)	≥1,200
Adaptable lunar slope (deg)	≤8
Horizontal landing velocity (m/s)	≤1
Vertical landing velocity (m/s)	≤4
Impact acceleration (g[b])	≤8
The degree of freedom	6
Movement speed (m/h)	≥100
Height of passable obstacles (mm)	250
Depth of passable obstacles (mm)	250

[a]Length × width.

[b]g is Earth's gravitational acceleration.

1. The landing legs of LMIG are folded and compacted during its launch process to meet the space requirements of the launch vehicle.
2. When the LMIG enters the circumlunar orbit, the landing legs are unfolded and locked to reduce the influence of engine exhaust plume and increase the landing stability.
3. Until the landing process, the landing legs keep unfold status and absorb the impact energy using buffer.
4. When the landing process is over, the orientation of landing legs is changed from point symmetry to bilateral symmetry for increasing the mobility of LMIG.
5. After the configuration transformation of landing legs, the LMIG starts lunar movement by using mechanical structures and control system.

Configurations of LMIG

Design of the deformation mechanism

As described in the previous section, the deformation mechanism is composed of fold–unfold mechanism (Fig. 3) and configuration–transfer mechanism (Fig. 4). The fold–unfold mechanism mainly consists of connector, driver spring, sliding rail, and locking mechanism. The connector is used to fix itself on configuration–transfer mechanism, and the locking mechanism can provide hinge joints for landing leg. In fold status, the locking mechanism is located at the top of the sliding rail, which is locked by the spring bolt and slot on the sliding rail. Meanwhile, the driver spring is compressed, and the landing legs are folded. In unfold status, the locking mechanism unlocks the spring bolt, and the landing leg unfolds along the sliding rail with the actuation of driving spring and locked again as it moves to the bottom of the sliding rail. The fold and unfold status can be seen in Fig. 2.

The configuration–transfer mechanism consists of fixed hinge, rotation axis, and revolving stage, and the fold–unfold mechanism is installed on it. The fixed hinge is used to install the landing leg. The revolving stage can be driven by the drive unit to rotate around the rotation axis. After landing, the orientation of landing legs is changed from point symmetry to bilateral symmetry for increasing the mobility of LMIG by configuration–transfer mechanism. The landing–moving status can also be seen in Fig. 2.

Design of the cushioning-driving integrated landing leg

The cushioning-driving integrated landing leg is composed of landing leg (Fig. 5) and energy-absorbing driving integrated buffer (Fig. 6). The landing leg is a type of series–parallel hybrid mechanism and composed of push rod, leg rod, foot pad, and buffer. The push rod is driven by the primary buffer, and the leg rod is driven by two secondary buffers. Therefore, the single landing leg has three degrees of freedom and the LMIG has six degrees of freedom. The foot pad is connected with the leg rod through the ball hinge, and the orientation can be adjusted according to different terrain.

Both the primary buffer and secondary buffer are the energy-absorbing driving integrated buffer, which have both cushioning and driving functions. In cushioning status, the transferring mechanism keeps locking using slot and spring bolt. When the landing leg is impacted, the piston rod moves and compresses the cushioning material in the tube to achieve energy-absorbing and cushioning. In driving status, the transferring mechanism keeps unlocking, the driving motor drives the screw to rotate, and the screw nut drives the piston rod outward or inward. The three buffers can move together to achieve the movement of the landing leg.

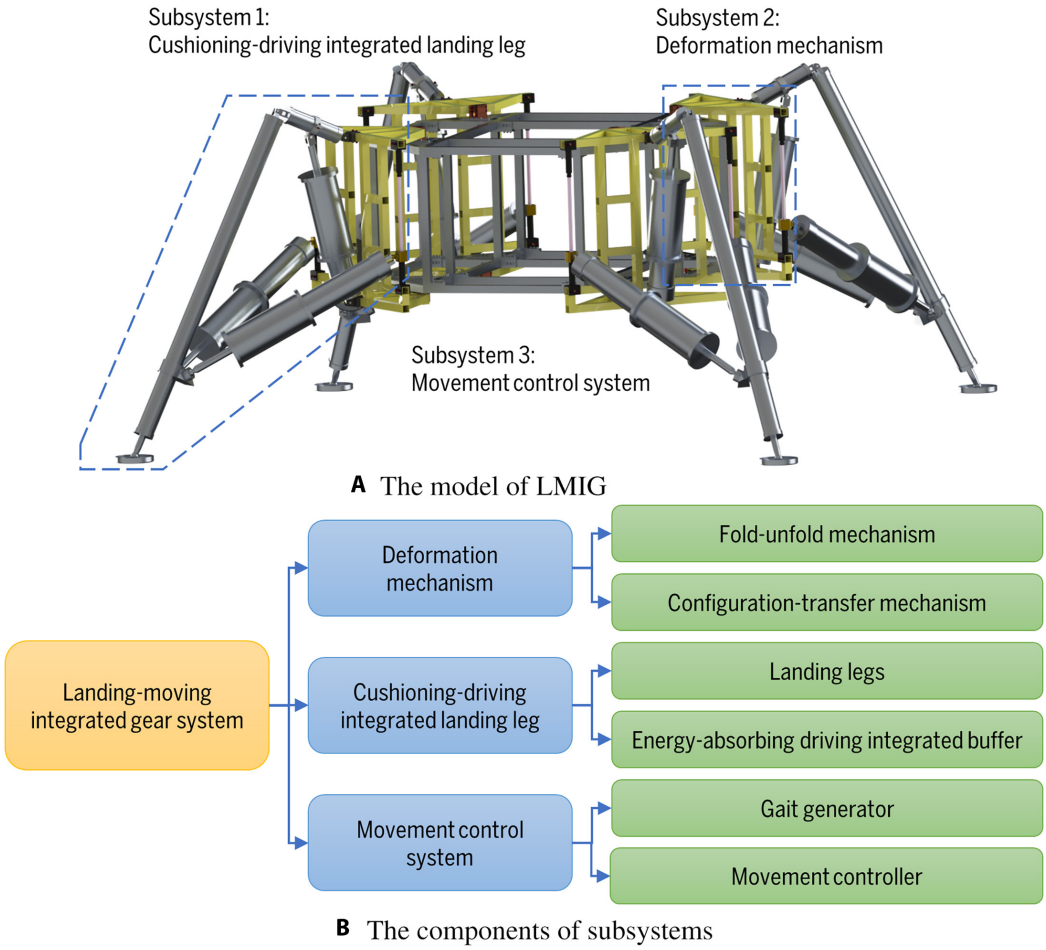

Fig. 1. (A and B) The compositions of LMIG system.

Design of the movement control system

The movement control system is shown in Fig. 7, which is composed of gait generator layer and movement control layer. In gait generator layer, the lunar environment and mission are used as inputs, and through trajectory planning, gait planning, and kinematics resolving, the driving motor angle sequence is obtained. Afterward, the driving trajectory is smoothed by filtering.

In movement control layer, the control architecture mainly controls the joints of landing leg. PID (proportion integration differentiation) control strategy is adopted for joint control, and velocity feedback, position feedback, and current feedback are led into the strategy to form a closed loop. Among them, velocity feedback is realized through the internal encoder of the motor, position feedback is realized through the external encoder of the joint, and the current feedback is realized through the current data read in motor driver. After that, the control strategy is adopted for all four landing legs to achieve precise movement control of LMIG.

Description and Analysis for the Cushioning Performance

Characteristic analysis of aluminum honeycomb

Effective energy-absorbing model of aluminum honeycomb

The antarafacial bearing capacity of aluminum honeycomb material is greater than the coplanar bearing capacity [45], so it is usually used as an energy-absorbing material to bear the antarafacial load in z direction, as shown in Fig. 8A. In this paper, hexagonal aluminum honeycomb is selected as the material of the buffer. The parameters of it mainly include a cell angle of α, a cell side length of l and w, and a cell wall thickness of t, as shown in Fig. 8B. Since the structure of the hexagonal aluminum honeycomb is symmetrical, the triangle shadow part in Fig. 8B is taken as the basic unit for study, and its size parameters are defined as shown in Fig. 8C.

In order to obtain the energy-absorbing characteristics of aluminum honeycomb materials and facilitate the design of buffer, the total effective energy-absorbing formulation of Y-cell is deduced by Eqs. 1 to 4.

$$W_{\text{total}} = \sigma_{\text{m}} S \varepsilon_{\text{D}} L \tag{1}$$

$$\sigma_{\text{m}} = \frac{\frac{\sqrt{3}}{3}\pi\sigma_0 t^2 l + \frac{2\sqrt{3}}{3}\pi\sigma_0 t^2 w}{k\sqrt{\frac{\sqrt{3}}{6}\pi t l + \frac{\sqrt{3}}{3}\pi t w(l\cos\alpha(w + l\sin\alpha))}} \tag{2}$$

$$\varepsilon_{\text{D}} = 1 - k_1 \frac{t}{\sqrt{\frac{\sqrt{3}}{6}\pi t l + \frac{\sqrt{3}}{3}\pi t w}} \tag{3}$$

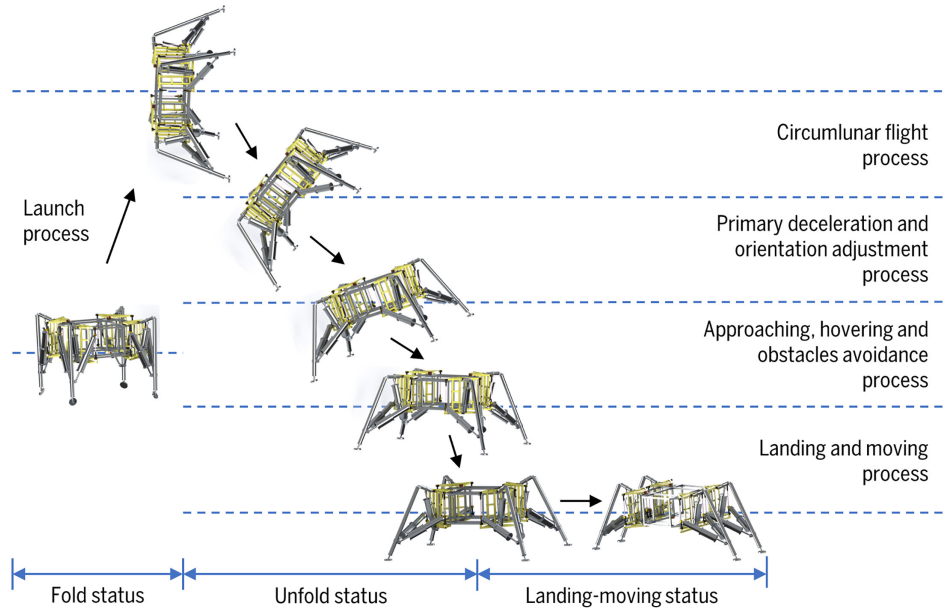

Fig. 2. The working procedure of LMIG.

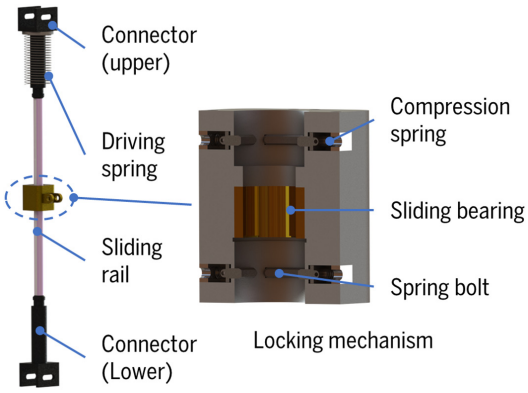

Fig. 3. The compositions of fold–unfold mechanism.

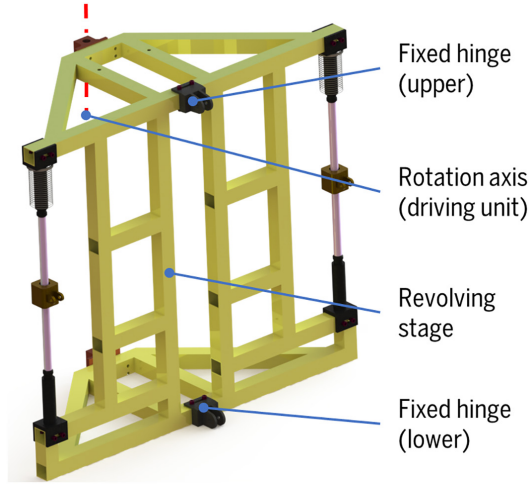

Fig. 4. The compositions of configuration–transfer mechanism.

$$S = l\cos\alpha(w + l\sin\alpha) \tag{4}$$

where the W_{total} is the total absorbed energy, σ_m is the average stress equation that can be derived from von Mises yield criterion, ε_D is the ultimate strain under antarafacial load, S is the area of Y-cell, L is the initial height of aluminum honeycomb, σ_0 is the initial yield strength, k is the coefficient of effective compression travel, k_1 is the coefficient of altimetric compensation.

Because the aluminum honeycomb has similar structure to Y-cell, the effective energy absorption formula of single-stage aluminum honeycomb can be obtained by Eq. 5.

$$W = \frac{S}{\frac{\pi}{4}\left(d_e^2 - d_i^2\right)}\sigma_m S\varepsilon_D L \tag{5}$$

where W is the total absorbed energy of single stage of aluminum honeycomb, and d_e and d_i are the external diameter and internal diameter of aluminum honeycomb, respectively.

Quasi-static compression test

In order to verify the accuracy of the established model, quasi-static compression tests on three different sizes of aluminum honeycomb materials are carried out by using MTS (mechanical testing and simulation) testing machine. The parameters of aluminum honeycomb are shown in Table 2. In this test, the aluminum honeycomb is fixed by two pressure plates, and the loading plate compresses down at a speed of 5 mm/min. The process and results of compression tests are shown in Figs. 9 and 10.

Under the condition of quasi-static compression, the loading–displacement curves of three sizes of aluminum honeycomb are obtained. The steady plastic deformation stage is taken as the research object since it is the main stage of energy-absorbing and the load fluctuation is stable. The average stress values and total absorbed energy values of three sizes of aluminum honeycomb materials are obtained. The comparison of theoretical and experimental results for them is

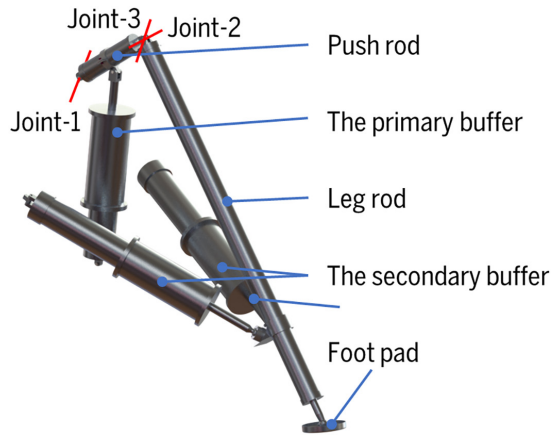

Fig. 5. The compositions of landing leg.

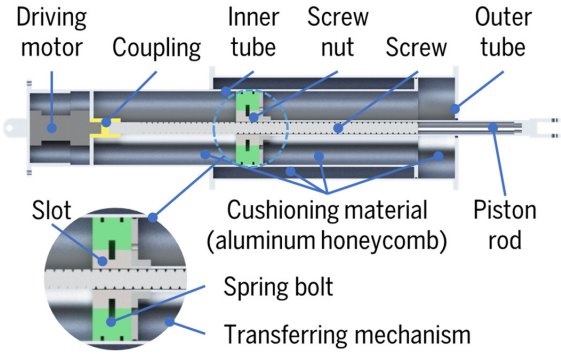

Fig. 6. The compositions of energy-absorbing driving integrated buffer.

shown in Tables 3 and 4. The difference between the theoretical and experimental results may be caused by material breakage during the tests, while the theoretical model does not consider the effect of material breakage. It can be seen from the tests that the deviation of the results is between 1.54% and 12.13%, which proves the validity of the theoretical model.

Characteristic analysis of multistage aluminum honeycomb buffer

Design of multistage aluminum honeycomb buffer

Multistage aluminum honeycomb buffer shows excellent cushioning performance, especially three-stage. In this paper, three sizes of aluminum honeycomb materials are selected as shown in Table 1. Based on the established quasi-static compression model of aluminum honeycomb, the dynamic impact model is further deduced with the Cowper–Symonds equation as a criterion.

$$W_{\text{total}}^{\text{d}} = \sigma_{\text{m}}^{\text{d}} S \varepsilon_{\text{D}} L \tag{6}$$

where v_0 is the velocity of landing impact, and D and p are the

$$\sigma_{\text{m}}^{\text{d}} = \frac{\frac{\sqrt{3}}{3}\pi\sigma_0 t^2 l + \frac{2\sqrt{3}}{3}\pi\sigma_0 t^2 w}{k\sqrt{\frac{\sqrt{3}}{6}\pi t l + \frac{\sqrt{3}}{3}\pi t w(l\cos\alpha(w + l\sin\alpha))}} \times \left[1 + \left(\frac{v_0}{8k_1 D\sqrt{\frac{\sqrt{3}}{6}\pi t l + \frac{\sqrt{3}}{3}\pi t w}}\right)^{\frac{1}{p}}\right] \tag{7}$$

sensitivity coefficients of the aluminum honeycomb material. Other parameters are the same as described before.

The primary buffer of landing leg is used to absorb the vertical impact load, so a single primary buffer is taken as the study object. A quarter of the load capacity of LMIG is selected as the impact load, and the three-stage buffer is used for antarafacial impact. The parameters of the three sizes of aluminum honeycomb are substituted into Eq. 6, and the following equation is obtained according to the law of conservation of energy.

$$W_1 + W_2 + W_3 = \frac{1}{2} m {v_0}^2 + mgh \tag{8}$$

$$h = L - k_1 \frac{tL}{H} \tag{9}$$

$$H = \sqrt{\frac{\sqrt{3}}{6}\pi t l + \frac{\sqrt{3}}{6}\pi t w} \tag{10}$$

where W_i is the absorbed energy by the aluminum honeycomb (1 for H004-3003, 2 for H005-3003, and 3 for H005-5052), m is a quarter of the load capacity of LMIG, and H is half height of the simplified folding unit of Y-cell.

Based on Eq. 8 and taking the length of aluminum honeycomb as the optimization objective, the objective function is established as follows.

$$F = f(L_1, L_2, L_3) \tag{11}$$

where Li is the length of aluminum honeycomb. The constraints are as follows.

1. Li is greater than 0 to ensure that the overload acceleration of LMIG will not change suddenly during the landing.
2. Li satisfies the requirement of energy conservation relation.
3. Li shall be as small as possible after compression to ensure that its cushioning performance is fully utilized.

The objective function is a linear programming problem, so the simplex method is used to solve it. After solving, the length of aluminum honeycomb is 90 mm ($L_1 = L_2 = L_3$). Considering the error between the theoretical compression rate and the actual compression rate, a safety margin value of 1.6 is introduced, and the length of the improved aluminum honeycomb is 120 mm.

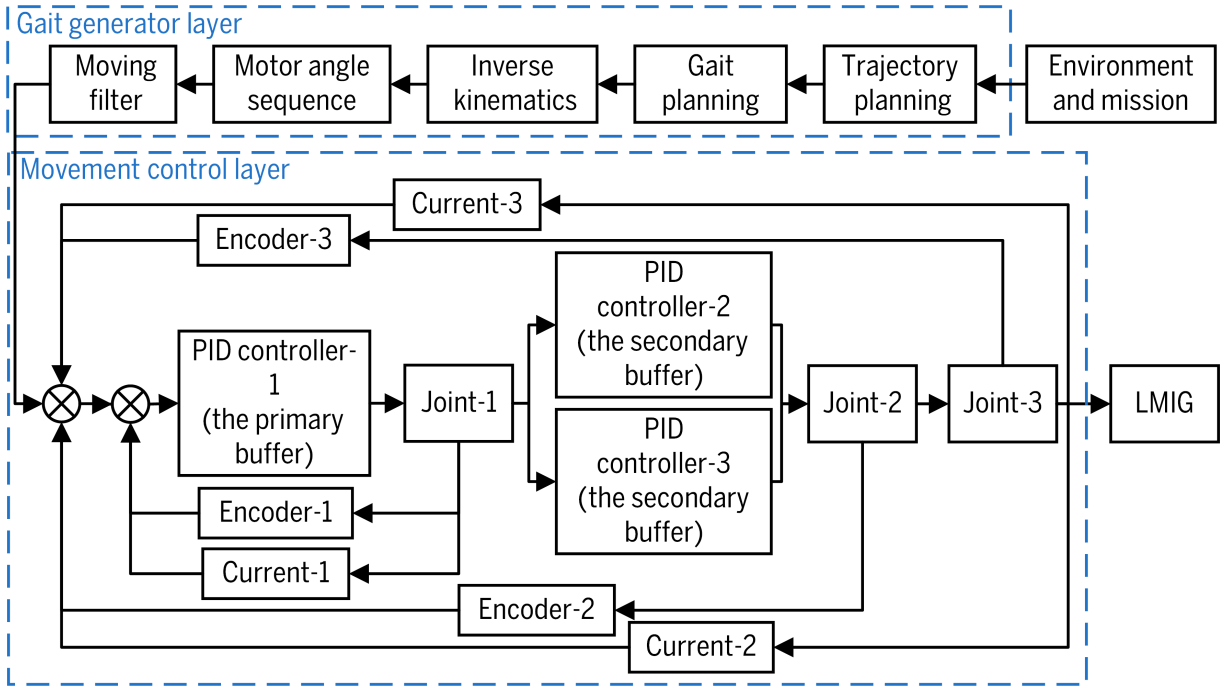

Fig. 7. The movement control system of LMIG.

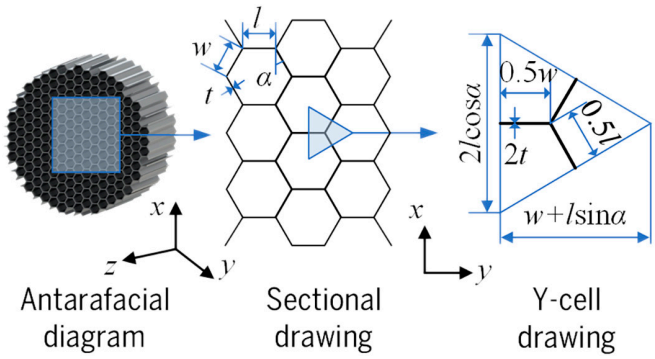

Fig. 8. The structure of hexagonal aluminum honeycomb.

Dynamic impact test

The designed three-stage aluminum honeycomb buffer is tested for dynamic impact using the CL-100 impact test bench. The length of aluminum honeycomb is shown in the optimization results in the previous section, and other parameters are consistent with Table 1. In this test, the mass load impacts the buffer at a speed of 4 m/s, the sampling frequency of the accelerometer is 8 kHz, and the test process and result are shown in Figs. 11 and 12.

From the test results, it can be seen that the aluminum honeycomb material is crushed and deformed in the order of "top to bottom," and the degree of deformation also decreases in this order. The remaining height of the buffer after compression is 100 mm, which is inaccurate compared with the theoretical value of 89 mm. The reason may be that the test bench is not rigidly connected to the ground and thus absorbs part of the energy. The overload acceleration curve during the test is shown in Fig. 13. It can be seen that the whole curve is smooth

Table 2. The parameters of aluminum honeycomb

Model	H004-3003	H005-3003	H005-5052
Y-cell thickness (t) (mm)	0.04	0.05	0.05
Y-cell length (l,w) (mm)	6	6	6
Y-cell angle (α) (rad)	$\pi/6$	$\pi/6$	$\pi/6$
Height (L) (mm)	100	100	100
Density (ρ) (kg/m^3)	30	36	50
Initial yield strength (σ_0) (MPa)	130	135	135
Elasticity modulus (E) (GPa)	40.39	41.02	41.73
External diameter (d_e) (mm)	184	184	184
Internal diameter (d_i) (mm)	50	50	50

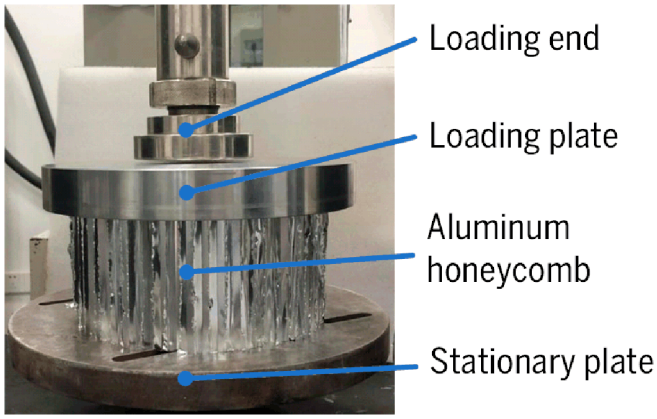

Fig. 9. Quasi-static compression test.

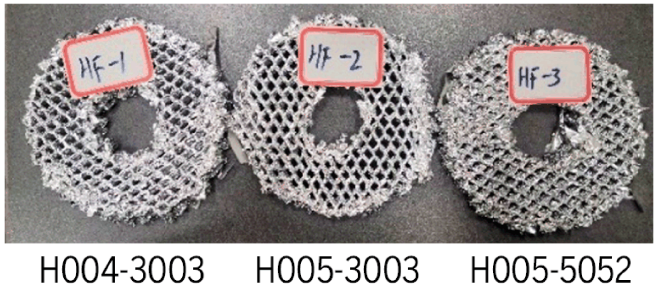

Fig. 10. The results of quasi-static compression test.

Table 3. The comparative results of average stress

Model	Theoretical value (GPa)	Experimental value (GPa)	Deviation (%)
H004-3003	0.2192	0.2361	7.16
H005-3003	0.3063	0.3111	1.54
H005-5052	0.3181	0.3282	3.08

Table 4. The comparative results of total absorbed energy

Model	Theoretical value (kJ)	Experimental value (kJ)	Deviation (%)
H004-3003	0.5325	0.4983	6.86
H005-3003	0.7366	0.6569	12.13
H005-5052	0.7649	0.6929	10.39

without mutation, and the maximum overload acceleration value is 6.1g (g is the Earth's gravitational acceleration), which meets the design requirement for maximum overload acceleration of LMIG.

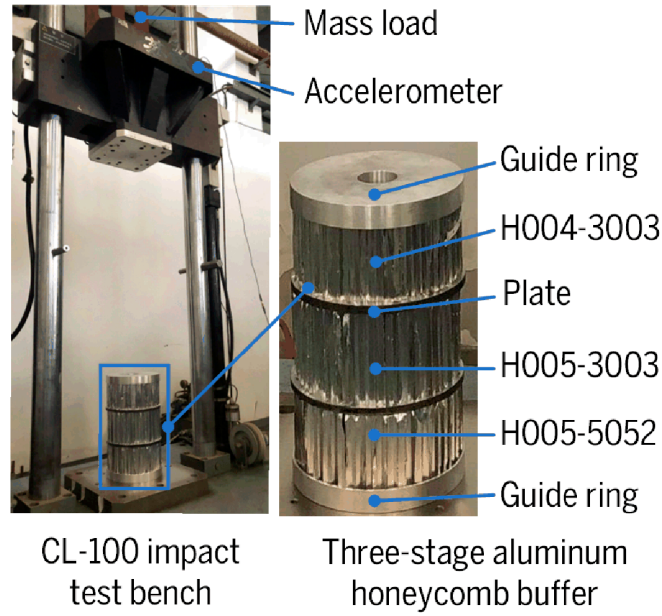

Fig. 11. Dynamic impact test.

Multi-load landing simulations of LMIG

In order to verify the effectiveness of the designed three-stage aluminum honeycomb buffer, a simplified model of LMIG is established in ADAMS software as shown in Fig. 14, and the parameters of the simplified model and the parameters between the footpad and the ground are shown in Tables 5 and 6, respectively. In this paper, the change of friction between the inner tube and the piston rod of the buffer is used to simulate the crushing force of multi-stage aluminum honeycomb buffer. As shown in Fig. 15, different cushioning forces can be simulated by changing the magnitude of the force in different stroke segments.

The landing simulations under different conditions are carried out, and the initial conditions are shown in Table 7. During the simulation, the touchdown speed (V_v) of LMIG is ensured by varying its height above the ground, and the gravitational acceleration is set to the lunar gravitational acceleration (1.63 m/s^2).

The simulation results are shown in Fig. 16. They show that the overload acceleration under all simulation conditions meets the design requirement, and the overload acceleration curve is smooth without mutation. The maximum overload acceleration value is 50 m/s^2. In summary, the simulation results show that the LMIG has good cushioning performance and can be effectively applied to the lunar surface landing.

Description and analysis for the movement performance

Kinematics and dynamic models

Kinematics model

Kinematics model is the basis of LMIG for movement navigation and control. In this paper, a single landing leg is taken as

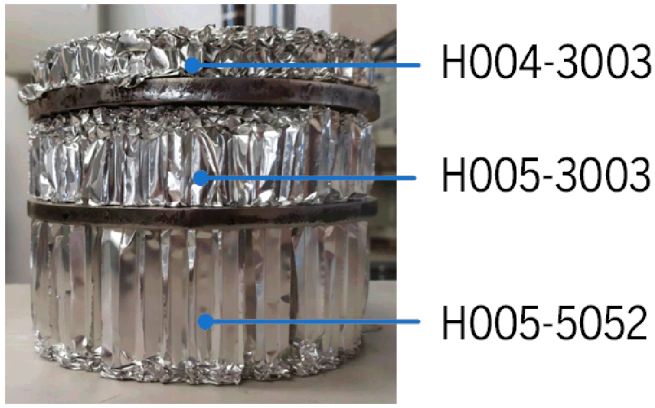

Fig. 12. The results of dynamic impact test.

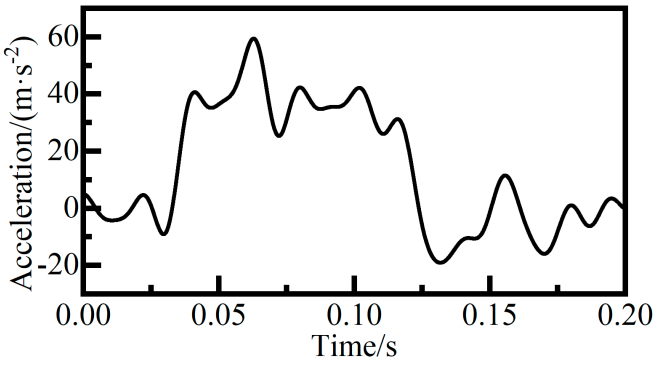

Fig. 13. The overload acceleration curve of dynamic impact test.

the object of study and its kinematics model is derived. Then, the single leg kinematics model is extended to LMIG by coordinate transformation. The single landing leg is a series–parallel hybrid configuration [(RPR)RU + 2UPS], consisting of a series kinematic chain (RU), a parallel kinematic chain (2UPS), and a closed triangular kinematic chain (RPR). The single leg has three degrees of freedom, which can be realized by one rotation hinge (θ_1) and one Hooke hinge (θ_2 and θ_3), as shown in Fig. 17A.

The joint frame of LMIG is defined according to the D–H (Denavit–Hartenberg) method as shown in Fig. 17B. The body frame $\{^{B}O\}$ is established at the geometric center of the body; the world frame $\{^{W}O\}$ is established at the projection of the geometric center of the body on the ground, with ^{W}y pointing to the direction of movement and ^{W}x pointing to the direction of gravity; the base frame ($\{^{i}O_0\}$, i = 1, 2, 3, 4, i indicates the serial number of four landing legs) of the single landing leg is established at the revolute joint (R1), with the direction of the three axes parallel to the direction of the body frame; the link frame ($\{^{i}O_1\}$, $\{^{i}O_2\}$ and $\{^{i}O_3\}$) is established at the revolute joints of the push rod and the leg rod, respectively; the foot-end frame $\{^{i}O_4\}$ is established at the end of the foot pad, and the spherical joint frame ($\{^{S}O_2\}$ and $\{^{S}O_3\}$) is established at the center of the spherical joints (S2 and S3). The link parameters of single landing leg are listed in Table 8.

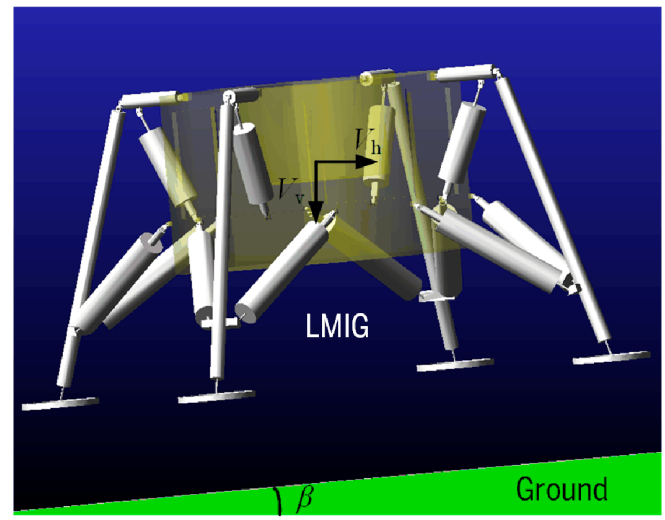

Fig. 14. The simplified model of LMIG.

Table 5. The parameters of simplified model

Components	Material	Mass (kg)	Size (mm)
Body	Steel	1,200	2,687 × 2,687 × 1,836 ($L \times W \times H$)
Push rod	Aluminum	10.80	150 × 690 ($D \times L$)
The primary buffer	Aluminum	26.30	285 × 1,563 ($D \times L$)
Leg rod	Aluminum	53.62	220 × 3,245 ($D \times L$)
The secondary buffer	Aluminum	45.66	285 × 1,820 ($D \times L$)
Foot pad	Aluminum	7.67	800 (D)
Ground	Wood	-	-

Table 6. The parameters between foot pad and ground

Parameters	Value
Contact stiffness (N·mm^{-1})	10^4
Damping coefficient (N·s·mm^{-1})	10^2
Penetration depth (mm)	0.1
Static friction coefficient	0.5
Dynamic friction coefficient	0.4

Substituting the link parameters into the link transformation (Eq. 12), the position and orientation transformation matrix between two adjacent links can be computed.

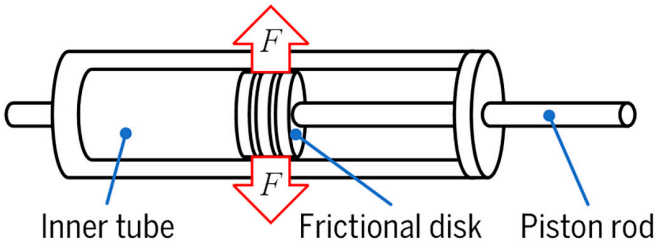

Fig. 15. The simulation of cushioning force.

Table 7. The landing simulations under different conditions

Case	Methods	V_v (m·s^{-1})	V_h (m·s^{-1})	β (°)
1	4 landing	4	0	0
2	4 landing	4	1	0
3	2-2 landing	4	0	8
4	2-2 landing	4	1	8
5	1-2-1 landing	4	0	8
6	1-2-1 landing	4	1	8

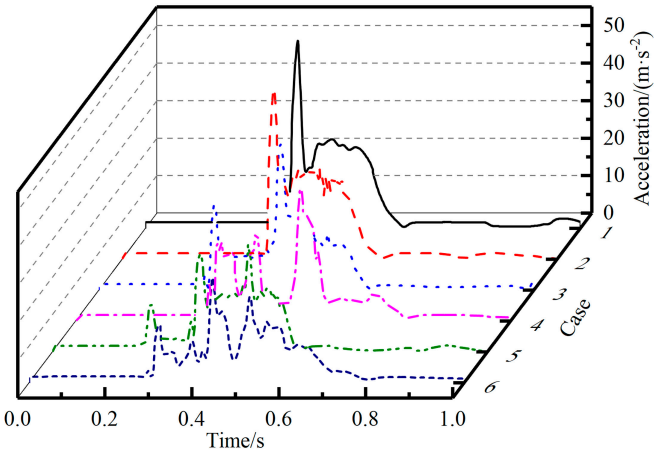

Fig. 16. The overload acceleration of landing simulations.

$$T_i^{i-1}=\begin{bmatrix}\cos\theta_i & -\sin\theta_i & 0 & a_{i-1}\\ \sin\theta_i\cos\alpha_{i-1} & \cos\theta_i\cos\alpha_{i-1} & -\sin\alpha_{i-1} & 0\\ \sin\theta_i\sin\alpha_{i-1} & \cos\theta_i\sin\alpha_{i-1} & \cos\alpha_{i-1} & 0\\ 0 & 0 & 0 & 1\end{bmatrix} \quad (12)$$

The forward kinematic solution of series kinematic chain (RU) can be obtained by multiplying the position and orientation transformation matrix of each link, as shown in Eqs. 13 and 14.

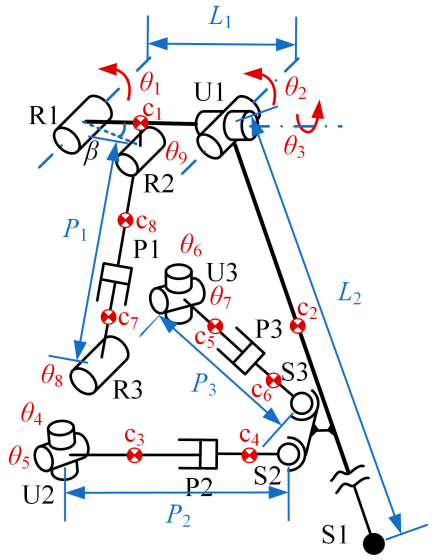

A The schematic diagram of mechanism for single landing leg

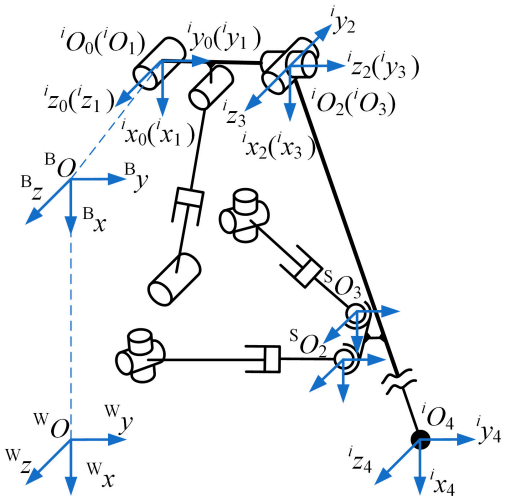

B The frames of single landing leg

Fig. 17. (A and B) The single landing leg of LMIG.

$$T_4^0=T_1^0T_2^1T_3^2T_4^3=\begin{bmatrix}r_{11} & r_{12} & r_{13} & p_x\\ r_{21} & r_{22} & r_{23} & p_y\\ r_{31} & r_{32} & r_{33} & p_z\\ 0 & 0 & 0 & 1\end{bmatrix} \quad (13)$$

$$\begin{cases}p_x=\cos\theta_1\cos\theta_2\cos\theta_3a_1-\sin\theta_1\sin\theta_3a_1-\sin\theta_1d_1\\ p_y=\sin\theta_1\cos\theta_2\cos\theta_3a_1+\cos\theta_1\sin\theta_3a_1+\cos\theta_1d_1\\ p_z=-\sin\theta_2\cos\theta_3a_1\end{cases} \quad (14)$$

The inverse kinematic solution of the landing leg can be obtained by separating the variables. First, the joint angle θ_1 is isolated to obtain Eq. 15.

$$\left[T_1^0(\theta_1)\right]^{-1}T_4^0=T_2^1(\theta_2)T_3^2(\theta_3)T_4^3 \quad (15)$$

Table 8. The link parameters of single landing leg

	Length (mm)		Twist (°)	Offset (mm)		Joint angle (°)	
Link	a_{i-1}	Value	α_{i-1}	d_i	Value	θ_i	Value
1	0	0	0	0	0	θ_1	0
2	0	0	–90	d_1	800	θ_2	0
3	0	0	90	0	0	θ_3	30
4	a_1	2,842	0	0	0	0	0

Writing the above equation in matrix form, Eq. 16 can be obtained.

$$\begin{bmatrix} \cos\theta_1 & \sin\theta_1 & 0 & 0 \\ -\sin\theta_1 & \cos\theta_1 & 0 & 0 \\ 0 & 0 & 1 & 0 \\ 0 & 0 & 0 & 1 \end{bmatrix} \begin{bmatrix} r_{11} & r_{12} & r_{13} & p_x \\ r_{21} & r_{22} & r_{23} & p_y \\ r_{31} & r_{32} & r_{33} & p_z \\ 0 & 0 & 0 & 1 \end{bmatrix} = \boldsymbol{T}_4^1 \tag{16}$$

Let the corresponding terms on both sides of the equal sign of Eq. 16 be equal. The system of Eq. 17 can be obtained.

$$\begin{cases} \cos\theta_1 p_x + \sin\theta_1 p_y = a_1 \cos\theta_2 \cos\theta_3 \\ -\sin\theta_1 p_x + \cos\theta_1 p_y = a_1 \sin\theta_3 + d_1 \\ p_z = -a_1 \sin\theta_2 \cos\theta_3 \end{cases} \tag{17}$$

The inverse kinematic solution for the series kinematic chain (RU) of the single landing leg can be computed by solving the above system of equations, as shown in Eqs. 18 and 19.

$$\begin{cases} \theta_1 = \arctan\left(\dfrac{p_y}{p_x}\right) - \arctan\left(\dfrac{K}{\pm\sqrt{{p_x}^2 + {p_y}^2 - K^2}}\right) \\ \theta_2 = \arcsin\left(\dfrac{p_z}{a_1 \cos\theta_3}\right) \\ \theta_3 = \arcsin\left(\dfrac{-\sin\theta_1 p_x + \cos\theta_1 p_y - d_1}{a_1}\right) \end{cases} \tag{18}$$

$$K = \frac{{p_x}^2 + {p_y}^2 + {p_z}^2 - {a_1}^2 + {d_1}^2}{2d_1} \tag{19}$$

After obtaining the forward and inverse kinematic solutions of the kinematic chain (RU), the mapping of the joint angle θ_1 and the active drive P_1 can be obtained from the closed triangular kinematic chain (RPR), as shown in Eq. 20, where β, $|R_1R_2|$, and $|R_1R_3|$ are fixed values.

$$\cos(\theta_1 + \beta) = \frac{|R_1R_2|^2 + |R_1R_3|^2 - |R_2R_3|^2}{2|R_1R_2||R_1R_3|} \tag{20}$$

The mapping of the joint angle (θ_1, θ_2) and the active drive (P_2, P_3) can be obtained in the kinematic chain (UPS) by solving the transformation matrix from the base frame $\{O_0\}$ to the spherical joint frame ($\{{}^{S}O_2\}$ and $\{{}^{S}O_3\}$) and the distance equation between the two points (U2 and S2, U3 and S3), as shown in Eq. 21.

$$\begin{cases} |U_2S_2| = \left\| \boldsymbol{P}^0_{S_{O_2}} - \boldsymbol{P}^0_{U_2} \right\| \\ |U_3S_3| = \left\| \boldsymbol{P}^0_{S_{O_3}} - \boldsymbol{P}^0_{U_3} \right\| \end{cases} \tag{21}$$

where $\boldsymbol{P}$ is the position vector, indicating the position of the joint point (S2, S3, U2, and U3) within the base frame $\{{}^{i}O_0\}$.

After that, the position and orientation transformation matrix between the body frame and the base frame of landing leg, and the position and orientation transformation matrix between the world frame and the body frame are computed in turn, and the forward and inverse kinematic solution of LMIG can be derived.

Dynamic model

Dynamic model plays an important role in designing motion metrics and guiding control system design of LMIG. In this paper, the dynamic model of single landing leg is derived by using Lagrange's equations of second kind. From the previous section, it is known that the landing leg is a series–parallel hybrid configuration. For modeling purposes, a single landing leg can be considered as a combination of eight independent rigid bodies, each with a center of mass denoted by c_1, …, c_8, as shown in Fig. 16A.

As an example, the kinetic and potential energy equations of push rod (*i*th rigid body) within the kinematic chain (RU) can be written in the following form.

$$\begin{cases} \boldsymbol{E}_{k1}(\boldsymbol{q}) = \frac{1}{2}\left({m_1}^0 \dot{\boldsymbol{p}}_1^T(\boldsymbol{q})\, {}^0\dot{\boldsymbol{p}}_1(\boldsymbol{q}) + \boldsymbol{\omega}_1^T \boldsymbol{I}_1 \boldsymbol{\omega}_1 \right) \\ \boldsymbol{E}_{p1}(\boldsymbol{q}) = {m_1}^0 \boldsymbol{g}^T \boldsymbol{p}_1(\boldsymbol{q}) \end{cases} \tag{22}$$

where $\boldsymbol{E}_{ki}$ and $\boldsymbol{E}_{pi}$ are the kinetic energy and potential energy of the *i*th rigid body, respectively; $\boldsymbol{q}$ is a generalized coordinate; m_i is the mass of the *i*th rigid body; ${}^0\boldsymbol{p}_1$ is the position values of the center of mass of the *i*th rigid body in the base frame; $\boldsymbol{\omega}_i$ is the angular velocity vector; $\boldsymbol{I}_i$ is the moment of inertia of the *i*th rigid body; ${}^0\boldsymbol{g}$ is the acceleration of gravity vector.

After that, substituting Eq. 22 into the Lagrange's equations of second kind gives the following form.

$$\boldsymbol{\tau}_1 = \boldsymbol{D}_1(\boldsymbol{q})\ddot{\boldsymbol{q}} + \dot{\boldsymbol{q}}^{\mathrm{T}} * \boldsymbol{H}_1(\boldsymbol{q})\dot{\boldsymbol{q}} + \boldsymbol{G}_1(\boldsymbol{q}) \tag{23}$$

where $\boldsymbol{\tau}_i$ is the generalized driving force vector of the *i*th rigid body; $\boldsymbol{D}_i$ is the inertial matrix of the *i*th rigid body; $\boldsymbol{H}_i$ is the cubic Hessian matrix of the *i*th rigid body; $\boldsymbol{G}_i$ is the gravity term.

Similarly, the dynamic equations for the other rigid bodies can be derived as follows.

$$\boldsymbol{\tau}_2 = \boldsymbol{D}_2(\boldsymbol{q})\ddot{\boldsymbol{q}} + \dot{\boldsymbol{q}}^{\mathrm{T}} * \boldsymbol{H}_2(\boldsymbol{q})\dot{\boldsymbol{q}} + \boldsymbol{G}_2(\boldsymbol{q}) \tag{24}$$

$$\begin{aligned} \boldsymbol{\tau}_k = {} & \boldsymbol{J}_j^T(\boldsymbol{q}, \boldsymbol{q}_1)\boldsymbol{D}_k(\boldsymbol{q})\boldsymbol{J}_j(\boldsymbol{q}, \boldsymbol{q}_1)\ddot{\boldsymbol{q}} + \dot{\boldsymbol{q}}^{\mathrm{T}} \\ & * \left(\boldsymbol{J}_1^T(\boldsymbol{q}, \boldsymbol{q}_1) \left(\boldsymbol{D}_k(\boldsymbol{q}) * \boldsymbol{H}_j(\boldsymbol{q}) + \boldsymbol{J}_j^T(\boldsymbol{q}, \boldsymbol{q}_1) * \boldsymbol{H}_k(\boldsymbol{q}) \boldsymbol{J}_j(\boldsymbol{q}, \boldsymbol{q}_1) \right) \right) \\ & \dot{\boldsymbol{q}} + \boldsymbol{J}_j^T(\boldsymbol{q}, \boldsymbol{q}_1)\boldsymbol{G}_k(\boldsymbol{q}) \end{aligned} \tag{25}$$

$$\begin{cases} j=1, & k=3,4 \\ j=2, & k=5,6 \\ j=3, & k=7,8 \end{cases} \tag{26}$$

Combining Eqs. 23 to 26, the dynamic equations are as follows:

$$\begin{aligned} \tau_{\mathrm{F}} = & \boldsymbol{D}_{\mathrm{F}}\left(\boldsymbol{q}_{\mathrm{F}}, \boldsymbol{q}, \boldsymbol{q}_1, \boldsymbol{q}_2, \boldsymbol{q}_3\right)\ddot{\boldsymbol{q}}_{\mathrm{F}} + \dot{\boldsymbol{q}}^{T} \\ & * \boldsymbol{C}_{\mathrm{F}}\left(\boldsymbol{q}_{\mathrm{F}}, \boldsymbol{q}, \boldsymbol{q}_1, \boldsymbol{q}_2, \boldsymbol{q}_3, \dot{\boldsymbol{q}}_{\mathrm{F}}\right)\dot{\boldsymbol{q}}_{\mathrm{F}} \\ & + \boldsymbol{G}_{\mathrm{F}}\left(\boldsymbol{q}_{\mathrm{F}}, \boldsymbol{q}, \boldsymbol{q}_1, \boldsymbol{q}_2, \boldsymbol{q}_3\right) \end{aligned} \tag{27}$$

where

$$\begin{aligned} & \boldsymbol{D}_{\mathrm{F}}\left(\boldsymbol{q}_{\mathrm{F}}, \boldsymbol{q}, \boldsymbol{q}_1, \boldsymbol{q}_2, \boldsymbol{q}_3\right) = \\ & \left(\left(J_{\mathrm{F}}^{-1}\left(\boldsymbol{q}, \boldsymbol{q}_{\mathrm{F}}\right)\right)^{\mathrm{T}} \boldsymbol{D}\left(\boldsymbol{q}, \boldsymbol{q}_1, \boldsymbol{q}_2, \boldsymbol{q}_3\right) J_{\mathrm{F}}^{-1}\left(\boldsymbol{q}, \boldsymbol{q}_{\mathrm{F}}\right)\right) \end{aligned} \tag{28}$$

$$\begin{aligned} & \mathbf{C}_{\mathrm{F}}\left(\boldsymbol{q}_{\mathrm{F}}, \boldsymbol{q}, \boldsymbol{q}_1, \boldsymbol{q}_2, \boldsymbol{q}_3, \dot{\boldsymbol{q}}_{\mathrm{F}}\right) = \dot{\boldsymbol{q}}_{\mathrm{F}}^{\mathrm{T}} * \\ & \left\{ \left[J_{\mathrm{F}}^{-1}\left(\boldsymbol{q}, \boldsymbol{q}_a\right)\right]^{\mathrm{T}} \left[J_{\mathrm{F}}^{-1}\left(\boldsymbol{q}, \boldsymbol{q}_{\mathrm{F}}\right)\right]^{\mathrm{T}} * \boldsymbol{H}\left(\boldsymbol{q}, \boldsymbol{q}_1, \boldsymbol{q}_2, \boldsymbol{q}_3\right) J_{\mathrm{F}}^{-1}\left(\boldsymbol{q}, \boldsymbol{q}_{\mathrm{F}}\right) \right. \\ & \left. - \left[J_{\mathrm{F}}^{-1}\left(\boldsymbol{q}, \boldsymbol{q}_{\mathrm{F}}\right)\right]^{\mathrm{T}} \left[J_{\mathrm{F}}^{-1}\left(\boldsymbol{q}, \boldsymbol{q}_{\mathrm{F}}\right)\right]^{\mathrm{T}} \boldsymbol{D}\left(\boldsymbol{q}, \boldsymbol{q}_1, \boldsymbol{q}_2, \boldsymbol{q}_3\right) J_{\mathrm{F}}^{-1}\left(\boldsymbol{q}, \boldsymbol{q}_{\mathrm{F}}\right) * \boldsymbol{H}_{\mathrm{F}}(\boldsymbol{q}) J_{\mathrm{F}}^{-1}\left(\boldsymbol{q}, \boldsymbol{q}_{\mathrm{F}}\right) \right\} \end{aligned} \tag{29}$$

$$\boldsymbol{G}_{\mathrm{F}}\left(\boldsymbol{q}_{\mathrm{F}}, \boldsymbol{q}, \boldsymbol{q}_1, \boldsymbol{q}_2, \boldsymbol{q}_3\right) = \left[J_{\mathrm{F}}^{-1}\left(\boldsymbol{q}, \boldsymbol{q}_{\mathrm{F}}\right)^{\mathrm{T}} * \boldsymbol{G}\left(\boldsymbol{q}, \boldsymbol{q}_1, \boldsymbol{q}_2, \boldsymbol{q}_3\right)\right] \tag{30}$$

$$\begin{cases} \boldsymbol{q}_{\mathrm{F}} = \left(\theta_1, P_2, P_3\right)^{\mathrm{T}} \\ \boldsymbol{q} = \left(\theta_2, \theta_3, \theta_1\right)^{\mathrm{T}} \\ \boldsymbol{q}_1 = \left(\theta_4, \theta_5, P_2\right)^{\mathrm{T}} \\ \boldsymbol{q}_2 = \left(\theta_6, \theta_7, P_3\right)^{\mathrm{T}} \\ \boldsymbol{q}_3 = \left(\theta_8, \theta_9, P_1\right)^{\mathrm{T}} \end{cases} \tag{31}$$

Thus, the dynamic equations for the single landing leg are derived, and the relationship between the input force and the output acceleration is obtained.

Gait planning and simulation

Unlike the conventional landers, the LMIG is equipped with functions such as surface movement and active posture adjustment, and gait planning is the basis for achieving the movement function. In the field of quadrupedal robots, gait is classified into static gait and dynamic gait depending on the duty cycle (the length of time that a single leg is in contact with the ground during the entire gait cycle). For LMIG, considering the high stability demand and high load demand during its movement, the static gait with high duty cycle is chosen as the walking gait. To reduce the number of posture adjustments in a single gait cycle, "LF-RF-RB-LB" is selected as the stepping sequence, with LF indicating the left front leg and RB indicating the right behind leg, and the others are similar. The longitudinal stability margin is proposed to evaluate the stability of LMIG during the movement, as shown in Fig. 18. The longitudinal stability margin is defined as the minimum value of the projection point of the COG of LMIG's body in the horizontal plane from the front and rear boundaries within the support polygon formed by the landing legs, and it can be written as

$$S_{\mathrm{M}} = \min\left\{D_{\mathrm{F}}, D_{\mathrm{B}}\right\} \tag{32}$$

Since the control strategy of LMIG is to control the three revolute joints of the single landing leg, a simplified model consisting of the kinematic chain (RU) is proposed as shown in Fig. 19. The projection frame $\{^{\mathrm{P}}O\}$ is established on the ground directly below the body frame $\{^{\mathrm{B}}O\}$, and the axes are oriented in the same direction as it did.

During the movement, it is necessary to ensure that the projection point of the COG of LMIG's body is always within the stable polygon and meets the stability margin requirement. Therefore, the stability judgment is based on the longitudinal stability margin, and the COG trajectory of LMIG is designed. The status before stepping of LMIG and its related parameters are shown in Fig. 20, W_{M} is the working space margin of the landing leg, and S_{M} is the longitudinal stability margin.

According to the stepping sequence and static gait planning of LMIG, the single gait cycle is divided into seven phases: PAP (posture adjustment phase), LF-stepping-phase, RF-stepping-phase, PAP, RB-stepping-phase, LB-stepping-phase, and PAP. Then, the COG trajectory of each phase is designed, the kinematic model is used to obtain the trajectory of each landing leg, and the whole gait can be generated. Since the LMIG adopts a lower moving speed, the segmented trigonometric function is used to design the COG trajectory in this paper. The segmented trigonometric trajectory can effectively ensure that the initial and ending velocities of the posture adjustment phase of LMIG are zero, and the functions of trajectory are given here as follows.

$$f(t) = \begin{cases} \boldsymbol{B}_1 \cos\left(\dfrac{\pi}{t_1 - t_0} t + \pi\right) + \boldsymbol{C}_1 & t \in \left[t_0, t_1\right] \\ \boldsymbol{B}_1 \cos\left(\dfrac{\pi}{t_1 - t_0} t_1 + \pi\right) + \boldsymbol{C}_1 & t \in \left(t_1, t_3\right) \\ \boldsymbol{B}_2 \cos\left(\dfrac{\pi}{t_4 - t_3} t + \pi\right) + \boldsymbol{C}_2 & t \in \left[t_3, t_4\right] \\ \boldsymbol{B}_2 \cos\left(\dfrac{\pi}{t_4 - t_3} t_4 + \pi\right) + \boldsymbol{C}_2 & t \in \left(t_4, t_6\right) \\ \boldsymbol{B}_3 \cos\left(\dfrac{\pi}{T - t_6} t + \pi\right) + \boldsymbol{C}_3 & t \in \left[t_6, T\right] \end{cases} \tag{33}$$

where $\boldsymbol{B}_1$ to $\boldsymbol{B}_3$ and $\boldsymbol{C}_1$ to $\boldsymbol{C}_3$ are parameter vectors of COG trajectory, determined by the boundary conditions during the movement; t_0 and t_1 are the starting and ending times of the initial posture adjustment phase, respectively; t_3 and t_4 are the starting and ending times of the second posture adjustment phase, respectively; t_6 is ending time of the last posture adjustment phase; T is the time of gait cycle.

The boundary conditions contain velocity conditions and position conditions to ensure the stability of LMIG moving

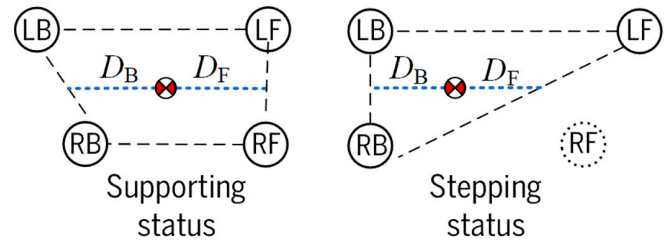

Fig. 18. The longitudinal stability margin.

process, the velocity boundary conditions are set to 0, and the position conditions are set as follows.

$$f(t)\Big|_{t=t_i} = \begin{pmatrix} {}^{\mathrm{PAP}}y_i \\ {}^{\mathrm{PAP}}z_i \end{pmatrix},\ i=0,1,\ \ldots,6,T \tag{34}$$

$${}^{\mathrm{PAP}}y_i = W_{\mathrm{M}} \tag{35}$$

$$\begin{cases} {}^{\mathrm{PAP}}z_i = {}^{\mathrm{G}}z_i - {}^{\mathrm{G}}z_{i-1} \\ {}^{\mathrm{G}}z_i - f_{\mathrm{LF-RB}}\left({}^{\mathrm{G}}y_i\right) = S_{\mathrm{M}} \\ {}^{\mathrm{G}}z_i - f_{\mathrm{RF-LB}}\left({}^{\mathrm{G}}y_i\right) = S_{\mathrm{M}} \end{cases} \tag{36}$$

The landing leg trajectory design is the basis for achieving posture adjustment and stepping. In this paper, the landing leg trajectory is divided into two parts: the posture adjustment trajectory and the stepping trajectory, as shown in Fig. 21. The trajectory equations are given as follows, where h is the step height, s is the step length, b_1 to b_3 are the tuning parameters, and α_{T} is the deflection angle of step.

$$\begin{cases} x(t) = \dfrac{-4h}{s^2}\left[b_1(t)\right]^2 + \dfrac{4h}{s}b_1(t) \\ y(t) = s\cos\alpha_{\mathrm{T}}b_2(t) \\ z(t) = s\sin\alpha_{\mathrm{T}}b_3(t) \end{cases} \tag{37}$$

In summary, the method of gait planning is divided into the following five steps.

1. Determining the parameters such as stability margins S_{M}, step length s, step height h, and deflection angle α_{T} for static gait planning.
2. Solving the COG trajectory according to the above parameters.
3. Solving for the landing leg posture trajectory and stepping trajectory based on the known COG trajectory.
4. Solving the displacement of the driving joints of LMIG using the kinematic model.
5. Output the "displacement–time" curve for each drive joint of LMIG.

In order to verify the correctness and effectiveness of the gait planning of LMIG, ADAMS software is used to simulate the designed static gait. To facilitate the subsequent tests of the

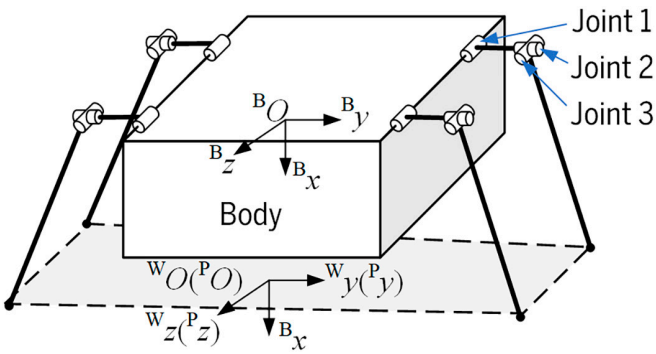

Fig. 19. The simplified model of LMIG.

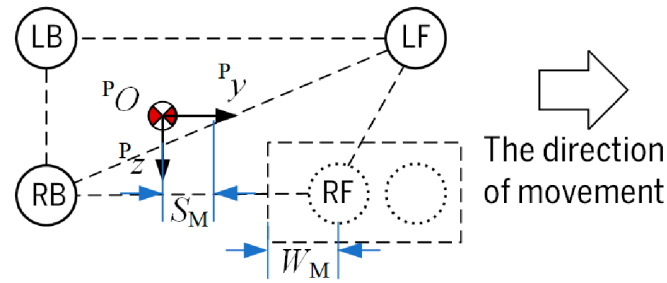

Fig. 20. The status before stepping of LMIG.

movement performance, a simplified scale model (1:2) for the simulation of LMIG is established, defining the direction of the world frame as shown in Fig. 22, with the ${}^{\mathrm{W}}x$ direction as the gravity direction and the ${}^{\mathrm{W}}y$ direction as the forward direction. The configuration parameters of LMIG are shown in Table 9.

In the walking gait simulation, the LMIG is set to have a single gait cycle time of 16 s, a step length of 40 mm, a step height of 60 mm, and a minimum stability margin of 100 mm. The simulation process of the walking gait for LMIG is shown in Fig. 23, and the body displacement, velocity, posture, and stability margin curves of LMIG are shown in Fig. 24.

From the simulation results, it can be seen that there is a small undulation of LMIG's body during the movement process, and the undulation displacement is 40 mm, accounting for about 3.44% of the height of LMIG; in the forward direction, the LMIG is fluctuating due to the existence of posture adjustment, and the moving speed is about 2.8 mm/s, which meets the requirement of design; in the lateral direction, the LMIG's body does not show a large deflection. The minimum stability margin is greater than the design requirement of stability margin (100 mm); in terms of velocity, within a single gait cycle, in the forward direction and lateral direction, the starting and ending velocity of LMIG is 0; in the vertical direction, the initial velocity is not 0 due to the presence of initial disturbance; the whole velocity-time curve is smooth without mutation. In terms of body posture change, the LMIG's body does not show large undulations and deflections during the movement.

Trajectory planning and optimization

In order to reduce the jerk and vibration of the landing leg during the stepping phase, the drive trajectory of the landing leg is optimized with the goal of "jerk-time." The drive trajectory is generated in the joint space of the landing leg and consists of many nodes. For the convenience of representing the displacement, jerk, and time of the driving trajectory, the cubic spline curve is chosen to describe the trajectory. According to the definition of the cubic spline curve, the expression of its Lagrange form is as follows.

$$\begin{cases} S_{ij}(t) = M_{ij}\dfrac{\left(t_{j+1}-t\right)^3}{6h_j} + \left(y_{ij} - \dfrac{M_{ij}h_j^2}{6}\right)\dfrac{t_{j+1}-t}{h_j} + M_{i,j+1}\dfrac{\left(t-t_j\right)^3}{6h_j} + \left(y_{i,j+1} - \dfrac{M_{i,j+1}h_j^2}{6}\right)\dfrac{t-t_j}{h_j} \\ \ddot{S}_{ij}(t) = -M_{ij}\dfrac{1}{h_j} + M_{i,j+1}\dfrac{1}{h_j} \end{cases} \tag{38}$$

$$M_{ij} = \ddot{S}_{ij}\left(t_j\right), M_{i,j+1} = \ddot{S}_{ij}\left(t_{j+1}\right), y_{ij} = S_{ij}\left(t_j\right), y_{i,j+1} = S_{ij}\left(t_{j+1}\right), h_j = t_{j+1} - t_j$$
$$\left(t \in \left[t_j, t_{j+1}\right]; i = 1, \ldots, N; j = 0, \ldots, n\right) \tag{39}$$

where $S_{ij}(t)$ is the displacement of the joint i in the time interval $[t_j, t_{j+1}]$; y_{ij} is the displacement of the joint i at the jth interpolation point in the time interval $[t_j, t_{j+1}]$; h_j is the time interval between t_j and t_{j+1}; t_j is time point; $i = 1, \ldots, N$ means there are N driving joints; $j = 0, \ldots, n$ means there are $n + 1$ interpolation points.

The driving trajectory planning of landing leg for LMIG has four constraints—velocity constraint, acceleration constraint, jerk constraint, and time constraint—and they can be described as follows.

$$\begin{cases} \left|\dot{S}_{ij}(t)\right| \le V_i, \max \\ \left|\ddot{S}_{ij}(t)\right| \le A_i, \max \\ \left|\dddot{S}_{ij}(t)\right| \le J_i, \max \\ h_{j,\min} \le h_j \le h_{j,\max} \end{cases} \tag{40}$$

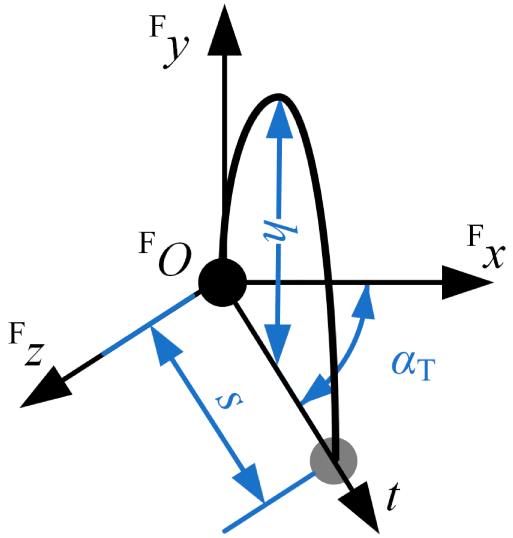

Fig. 21. The landing leg trajectory of LMIG.

In order to reduce the jerk of the joints in the landing leg motion and increase the stability of the movement process and the service life of the mechanism, the objective function of the optimization model with "jerk-time" as the optimization objective is as follows.

$$F\left(h_j\right) = N\sum_{j=0}^{n} h_j + N\sum_{j=0}^{n}\left(\left| -M_{ij}\frac{1}{h_j} + M_{i,j+1}\frac{1}{h_j}\right|\right) \tag{41}$$

In the process of trajectory optimization, an optimization model with time interval as the design variable needs to be established; however, to obtain a smooth driving trajectory, more interpolation points will inevitably be introduced, which brings more design variables. For this reason, this paper uses MSGA (multiple swarm genetic algorithm) as the optimization algorithm, which has the following advantages. The flow chart of the algorithm is shown in Fig. 25.

1. Lower requirements for the objective function and constraints, and better adaptability to optimization problems.

2. Highly capable of solving multi-objective optimization problems, as multi-objective parallel operations can be performed.

3. Different populations can be given different control parameters, and individuals can be exchanged among various populations, thus facilitating the synergistic evolution of multiple populations and avoiding falling into local optimal solutions.

Combined with the stepping parameters of landing leg, the trajectory sampling points are set to 9, the stepping trajectory is sampled uniformly, and the mapping points of the drive trajectory for the drive joint are obtained by the kinematic model, as shown in Table 10. Among them, virtual nodes are introduced to ensure that the start and end values of velocity and acceleration are constant.

The parameters of MSGA were set as follows: the number of individuals is 200; the chromosome length of individuals is 20; the number of populations is 20; the maximum number of iterations is 200; the initial crossover probability is 0.8; the initial variation probability is 0.01; and the landing leg constraints are shown in Table 11.

The optimization is repeated five times using MSGA, the values of design variables for the best and worst results are recorded, and the results of optimization are shown in Table 12. The value of unoptimized design variables was set as the upper boundary value of the boundary condition.

Table 9. The parameters of simplified scale model of LMIG

Parameters	Value
Standing height (mm)	1,163.75
Total mass (kg)	1,149.24
Body size (mm)	1,600 × 1,600 × 835
Body mass (kg)	681.21
Push rod length (mm)	250
Leg rod length (mm)	1,300
Foot pad size (mm)	Φ120 × 14
The buffers initial length (mm)	769, 650, 650
The single leg mass (kg)	117.03

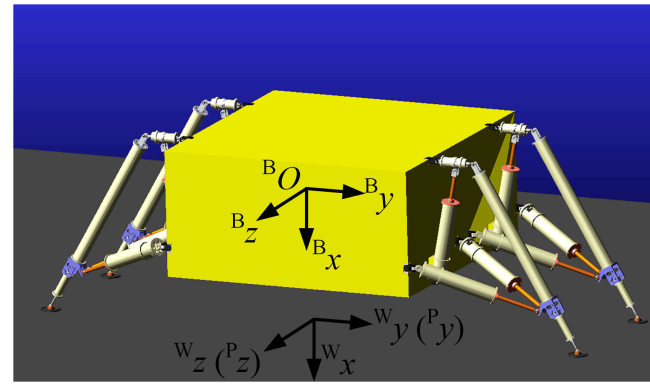

Fig. 22. The simplified scale model of LMIG.

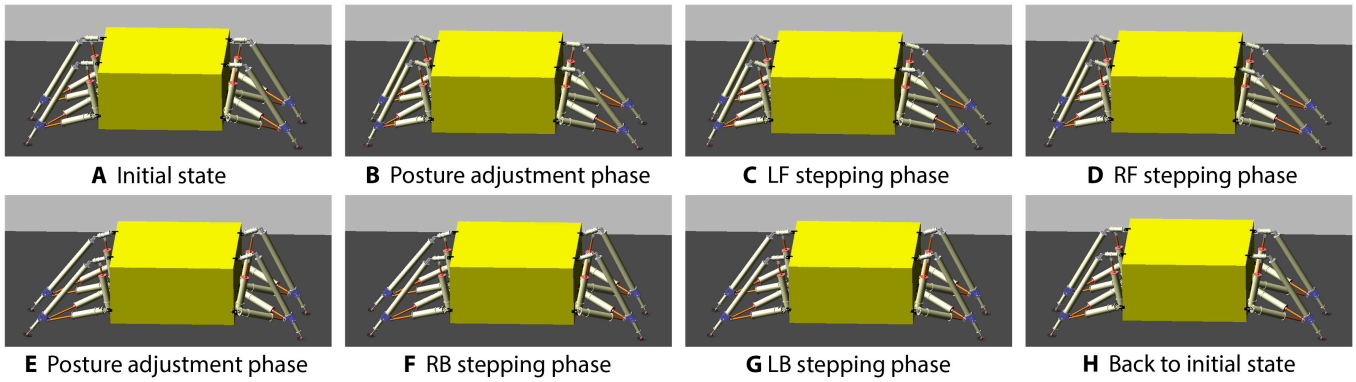

Fig. 23. The walking gait simulation of LMIG.

It can be seen from Table 12 that compared with the unoptimized trajectory, the jerk value of the optimized trajectory has been greatly reduced. The optimized trajectory achieves a comprehensive optimization of time and jerk, and reduces the jerk and vibration of the landing leg during the stepping phase while ensuring the speed of movement.

Prototype Ground Tests

Test for the cushioning performance

Based on the configuration design of LMIG, a prototype for cushioning test is developed as shown in Fig. 26. The body and deformation mechanism are made of steel, and the landing leg is made of aluminum alloy.

Due to the limitation of site and equipment, a single dimension drop test device is developed to carry out the cushioning performance test of a single landing leg, as shown in Fig. 27. The device can realize the single-leg landing test with different vertical speed and different landing slope. During the test, the acceleration change of the landing leg and the support reaction force change of the foot pad can be collected.

With the vertical landing speed of 4 m/s as the testing condition, the foot pad of the landing leg is calculated to be 190 mm above the ground according to the energy conversion method, and the landing leg is lifted to the specified height as shown in Fig. 28A. After the landing test, the state of the landing leg is shown in Fig. 28B, the parameter changes are shown in Table 13, and the overload acceleration change is shown in Fig. 29.

From the above results, it can be seen the lengths of the buffers all change during the cushioning process, and there is a small difference in the length of the two secondary buffers due to the sliding of the foot pad; the overload acceleration reaches a maximum of 6.5g (g is the Earth's gravitational acceleration) at 0.064 s, which is within the allowable range of the design requirements.

Test for the movement performance

In order to facilitate the movement test, a scaled (1:2) prototype for movement test is developed as shown in Fig. 30. The body and landing legs are made of aluminum alloy, and the load-carrying structure and reinforcement of body are made of steel. The parameters of the controller, encoder, and driver components are shown in Table 14.

Based on the control system design and gait planning design, movement test of the scaled prototype is conducted. The ground station initializes the scaled prototype through the position machine and sends the control commands through the remote controller. Then, the scaled prototype can move according to the commands.

The process of movement test is shown in Fig. 31. The test results show that the moving speed of the scaled prototype is 15 mm/s, and the moving speed of the full-scale prototype can be calculated as 108 m/h using the similarity rule, which meets the design requirements.

Conclusions

Cushioning and movement performance are important indicators for MLL. By the analysis of design requirements and constraints of LMIG, this paper presents an LMIG for MLL with excellent cushioning and movement performance. The main work is summarized as follows.

1. The composition of LMIG is given, and the fold–unfold mechanism, configuration–transfer mechanism, landing leg, energy-absorbing driving integrated buffer, and movement control system of LMIG are designed.

2. A three-stage aluminum honeycomb buffer is proposed, and the static compression and dynamic impact tests on aluminum honeycomb material are conducted to verify the effectiveness of the proposed buffer. The landing simulations of LMIG under various landing conditions are carried out. The results show that the proposed buffer design method is reasonable and effective, and the designed buffer of LMIG has excellent cushioning performance.

3. The kinematic and dynamic models of LMIG are established. The walking gait of LMIG is planned and simulated, and the results show that the designed gait is stable without large fluctuation and offset, and the driving trajectory of LMIG is optimized to reduce the jerk and vibration during the movement. The simulation results show that the designed gait planning and trajectory optimization method can significantly improve the stability and movement performance of LMIG.

4. The drop test of the single landing leg of LMIG is carried out, and the results show that LMIG has good cushioning performance with a maximum overload acceleration of 6.5g; the movement test of the scaled prototype of LMIG is carried out, and the results show that LMIG has good movement performance, and the moving speed can reach 108 m/h. The test results further show that the designed LMIG meets the design requirements and has excellent cushioning and movement performance.

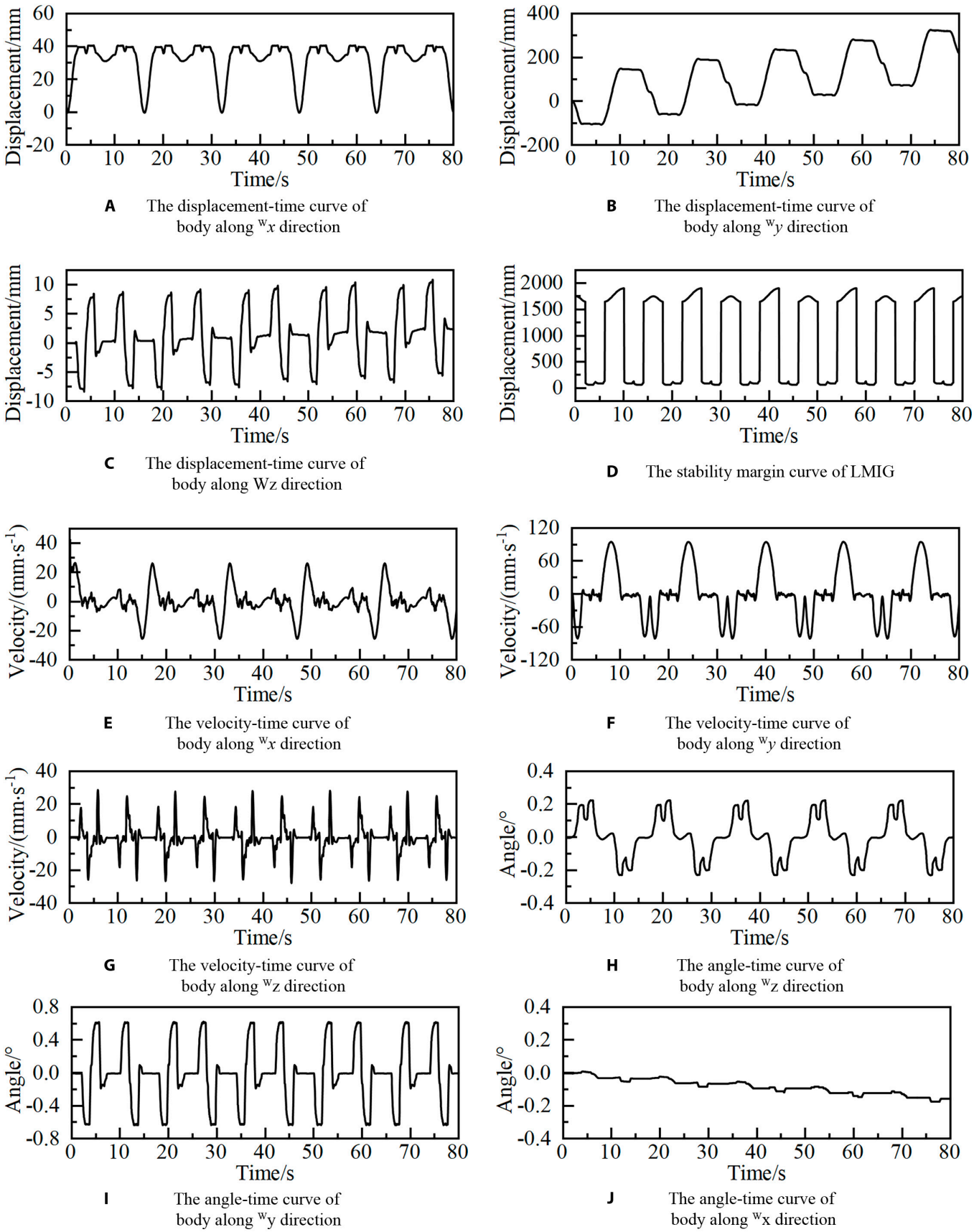

Fig. 24. (A to J) The simulation curves of LMIG.

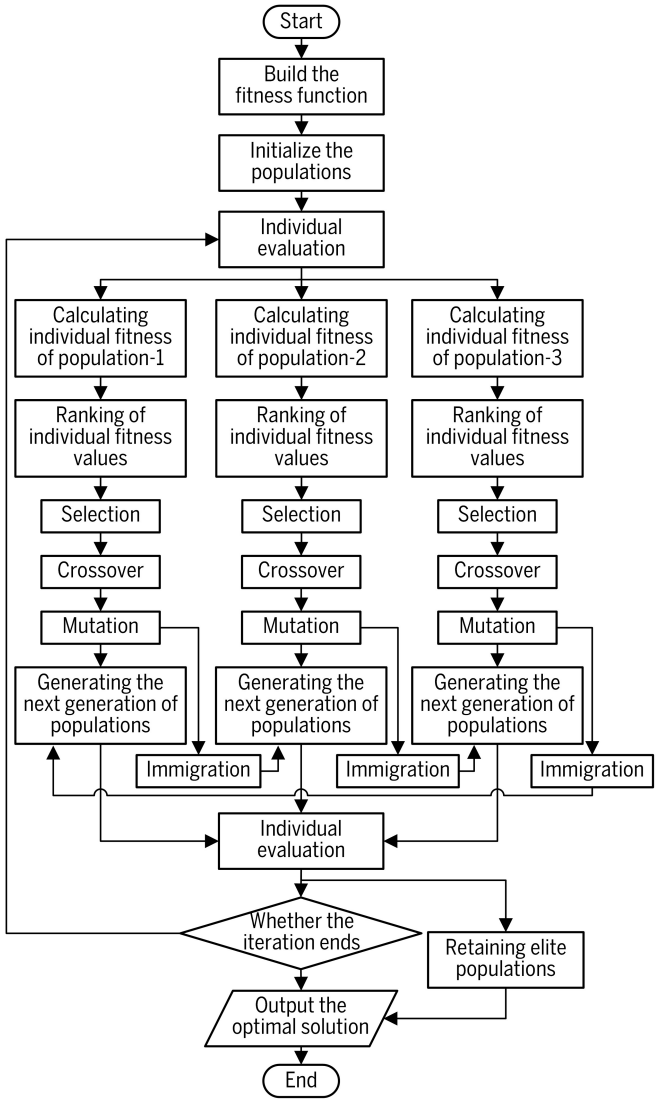

Fig. 25. The flow chart of the MSGA.

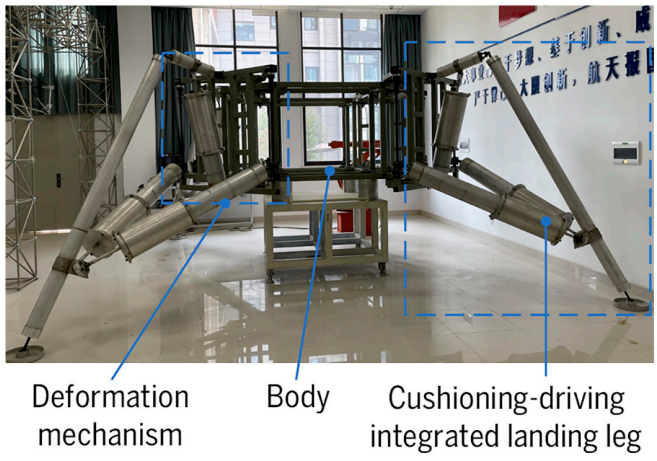

Fig. 26. The prototype of LMIG for cushioning.

In future work, we plan to further improve the ability of LMIG to move in complex terrain and improve the environmental sensing capability of LMIG by adding an environmental sensing system.

Table 10. The joints of stepping and driving trajectory

Points	Positions of stepping trajectory (mm)	Displacement of driving joint (mm)
1	(0, 0, 0)	(0, 0, 0)
2	Virtual node	Virtual node
3	(5, 26.25, 0)	(12.09, –9.90, –9.90)
4	(10, 45, 0)	(20.04, –15.12, –15.12)
5	(15, 56.25, 0)	(24.12, –16.49, –16.49)
6	(20, 60, 0)	(24.48, –14.46, –14.46)
7	(25, 56.25, 0)	(21.14, –9.12, –9.12)
8	(30, 45, 0)	(13.99, –0.21, –0.21)
9	(35, 26.25, 0)	(2.78, 12.93, 12.93)
10	Virtual node	Virtual node
11	(40, 0, 0)	(–12.98, 31.43, 31.43)

Table 11. The constraints of single landing leg

Constraints	Joint 1	Joint 2	Joint 3
$V_{i,max}$ (mm·s^{-1})	500	120	120
$A_{i,max}$ (mm·s^{-2})	1,500	600	600
$J_{i,max}$ (mm·s^{-3})	18,000	6,000	6,000
h_j (s)	[0.1, 0.2]	[0.1, 0.2]	[0.1, 0.2]

Table 12. The results before and after optimization

MSGA	The values of design variables (s)	Total time (s)	Total jerk (mm·s^{-3})
Best	{0.3711, 0.1570, 0.1501, 0.1501, 0.1500, 0.1523, 0.1635, 0.3999}	1.6940	30,185
Worst	{0.3704, 0.1604, 0.1932, 0.1685, 0.1975, 0.1636, 0.1829, 0.3961}	1.8328	37,599
None	{0.4, 0.2, 0.2, 0.2, 0.2, 0.2, 0.2, 0.4}	2	80,945

Acknowledgments

Funding: We would like to acknowledge the National Science and Technology Special Projects (grant nos. 2021-JCJQ-JJ-0233, 23-TQ01-04-ZT-01-017, and D050202), the Fundamental Research Funds for the Central Universities (grant no. NT2022026) and National Natural Science Foundation of China (General Program, grant no. 52075242) for the funding of this work.
Author contributions: X.Z. is responsible for overall coordination, manuscript writing, and data collection. C.N. provided

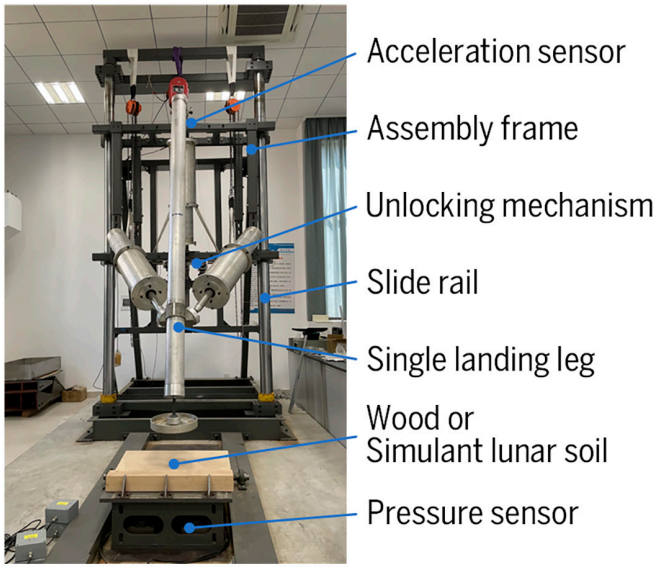

Fig. 27. The single dimension drop test device.

Fig. 28. (A and B) The single dimension drop test device.

Table 13. The results before and after test

Parameters	Before	After
The length of primary buffer (mm)	1,290	1,400
The length of secondary buffer (mm)	1,720	1,680
The length of secondary buffer (mm)	1,720	1,690
Angle between push rod and ground (deg)	0	20
Slip distance of foot pad (mm)	0	185

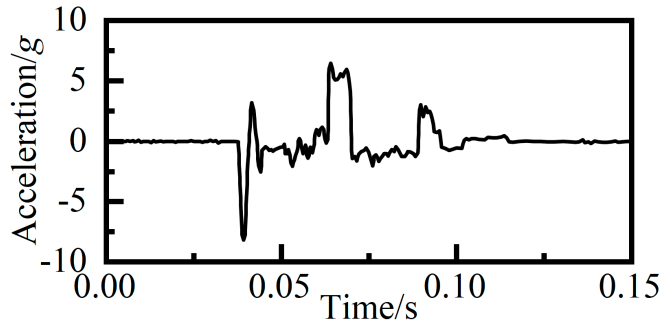

Fig. 29. The overload acceleration curve of test.

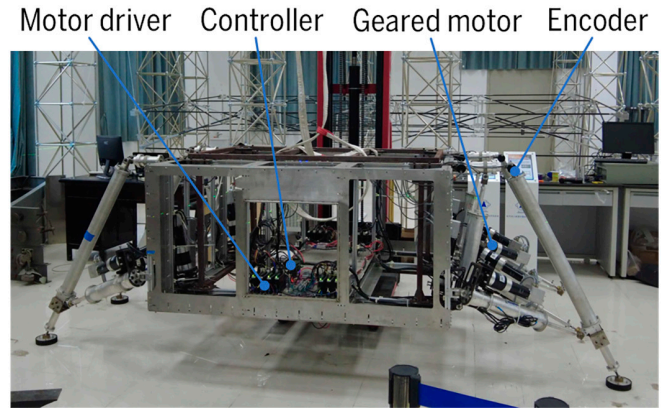

Fig. 30. The scale prototype of LMIG for movement.

Table 14. The parameters of controller and driver components

Components	Specifications	Value
Controller	Basic frequency (MHz)	767
	RAM (GB)	1
	Data transfer rate (Mbps)	1,066
	CAN Bus interface	2
	UART Bus interface	2
	Encoder interface	16
Encoder	Rated voltage (V)	5
	Rated current (mA)	160
	Resolution ratio ($p \cdot r^{-1}$)	2,000
	Response frequency (kHz)	100
Geared motor	Rated voltage (V)	48
	Rated current (A)	5.9
	Rated speed (rpm)	2,680
	Rated torque (mN·m)	543
	Reduction ratio	51:1
	Mass (kg)	6.1

data acquisition and contributed to the writing of the paper. S.J. provided supervisory support and technical guidance. J.C. is the supervisor of the investigation efforts and offered many valuable helps and suggestions. D.V.M. provided data acquisition

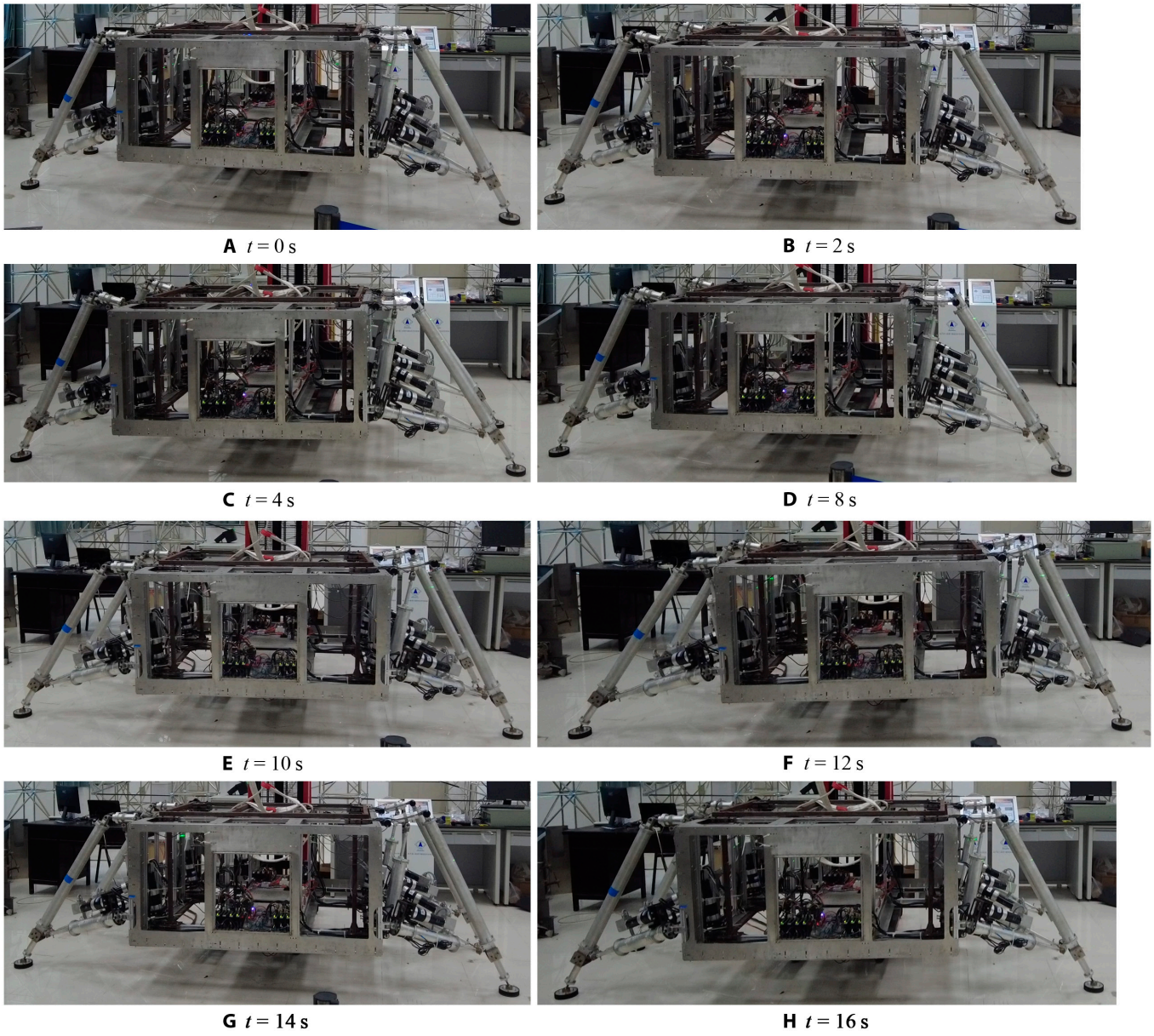

Fig. 31. (A to H) The movement test of LMIG.

and technical guidance. J.Z. provided supervisory support and data acquisition and contributed to the writing of the paper.
Competing interests: The authors declare that they have no competing interests.

Data Availability

The data used to support the findings of this study are included within the article.

References

1. Moisheev AA, Shirshakov AE. On the fiftieth anniversary of the launch of Luna-16, Luna-17, and Venera-7. *Sol Syst Res*. 2021;55:765–771.
2. Davies ME, Colvin TR. Lunar coordinates in the regions of the Apollo landers. *J Geophys Res*. 2000;105(8):277–280.
3. "Chinese probe lands on Moon to gather lunar samples (Update)," 2020, October 2022, https://phys.org/news/2020-12-chinese-probe-moon-lunar-samples.html
4. Benton MG. Spaceship discovery—Vehicle architecture for human exploration of moon, mars, and beyond, in Space 2006; 2006; San Jose, CA, USA.
5. Benton MG. Crew exploration lander for ganymede, callisto, and Earth's moon—Vehicle system design, in 45th AIAA Joint Propulsion Conference and Exhibit; 2009; Denver, CO, USA.
6. Kennedy KJ. Lunar lander strategies, in 11th Biennial ASCE Aerospace Division International Conference on Engineering, Science, Construction, and Operations in Challenging Environments; 2008; Long Beach, CA, USA.

7. Huang LY, Howe AS. A kit-of-parts approach to pressure vessels for planetary surface construction, in Space 2003; 2003; Long Beach, California, USA.
8. Mankins JC. Modular architecture options for lunar exploration and development. *Space Technol*. 2002;1(4):53–64.
9. Wilcox BH. ATHLETE: A mobility and manipulation system for the moon, in IEEE Aerospace Conference; 2007; Big Sky, MT, USA.
10. Zhang ZX, Liang L, Guo LL, Ye PJ. Conceptual design of manned lunar lander with wheel-legged mobile system. *Manned Spaceflight*. 2016;22(2):202–209.
11. Jia S, Zhou XH, Chen JB, et al. Kinematics research and gait planning of buffering/walking integrated lander. *J Astro*. 2021;42(4):467–476.
12. Jia S, Zhou XH, Chen JB, et al. System design and experimental verification of mobile lunar lander. *J Deep Space Explor*. 2021;42(4):467–476.
13. Lin RF, Guo WZ. Novel design of a family of legged mobile landers based on decoupled landing and walking functions. *J Mech Sci Technol*. 2020;34(9):3815–3822.
14. Lin RF, Guo WZ. Creative design of legged mobile landers with multi-loop chains based on truss-mechanism transformation method. *J Mech Sci Technol*. 2020;34(9):3815–3822.
15. Apollo 11 preliminary science report, 1969; https://www.hq.nasa.gov/alsj/a11/as11psr.pdf
16. Vinogradov AP. Preliminary data on lunar ground brought to Earth by automatic probe 'Luna-16'", in Proceedings of the Lunar Science Conference; 1971; Houston, TX, USA.
17. Ye PJ, Sun ZZ, Zhang H, Zhang L, Wu X, Li F. Mission design of Chang'e-4 probe system. *Sci Sin Tech*. 2019;49(2):124–137.
18. Luo CJ, Zhou AL, Liu RQ, et al. Average compressive stress constitutive equation of honeycomb metal under out-of-plane compression. *J Mech Eng*. 2010;46(18):52–59.
19. Zheng ZJ, Yu JL, Li JR. Dynamic crushing of 2D cellular structures: A finite element study. *Int J Impact Eng*. 2005;32(1):650–664.
20. Li XC, Lin YL, Lu FY. Numerical simulation on in-plane deformation characteristics of lightweight aluminum honeycomb under direct and indirect explosion. *Materials*. 2019;12(14):2222.
21. Ashab AA, Ruan D, Lu GX, Bhuiyan AA. Finite element analysis of aluminum honeycombs subjected to dynamic indentation and compression loads. *Materials*. 2016;9(3):162.
22. Khan MK, Baig T, Mirza S. Experimental investigation of in-plane and out-of-plane crushing of aluminum honeycomb. *Mater Sci Eng A*. 2012;539:135–142.
23. Wang ZG, Tian HQ, Lu ZJ, Zhou W. High-speed axial impact of aluminum honeycomb – Experiments and simulations. *Compos Part B Eng*. 2014;56:1–8.
24. Duan D, Lu G, Wang B, Yu TX. In-plane dynamic crushing of honeycombs—A finite element study. *Int J Impact Eng*. 2003;28(2):161–182.
25. Yildiz AR. A comparative study of population-based optimization algorithms for turning operations. *Inf Sci*. 2012;210:81–88.
26. Zhang Y, Lu MH, Wang CH, Sun G, Li G. Out-of-plane crashworthiness of bio-inspired self-similar regular hierarchical honeycombs. *Compos Struct*. 2016;144:1–13.
27. Sun DQ, Zhang WH, Wei YB. Mean out-of-plane dynamic plateau stresses of hexagonal honeycomb cores under impact loadings. *Compos Struct*. 2010;92(11):2609–2621.
28. Chen JB, Qian JC, Jia S, et al. Research and analysis of cushioning performance of new multistage aluminum honeycomb buffer. *J Northwest Polytech Univ*. 2020;38:1–6.
29. Nohmi M, Miyahara A. Modeling for lunar lander by mechanical dynamics software, in AIAA Modeling and Simulation Technologies Conference and Exhibit; 2005; San Francisco, CA, USA.
30. Lavender RE. On touchdown dynamics analysis for lunar lander, in Symposium on Structural Dynamics and Aeroelasticity; 1965; Boston, MA, USA.
31. Han YC, Guo WZ, Peng ZK, et al. Dimensional synthesis of the reconfigurable legged mobile lander with multi-mode and complex mechanism topology. *Mech Mach Theory*. 2020;155:Article 104097.
32. Yin K, Sun Q, Gao F, Zhou SL. Lunar surface soft-landing analysis of a novel six-legged mobile lander with repetitive landing capacity. *J Mech Eng Sci*. 2021;236(2):1–20.
33. Temirbekov ES, Bostanov BO, Dudkin MV, Kaimov ST, Kaimov AT. Combined trajectory of continuous curvature, in The International Conference of IFToMM ITALY; 2019; Cassino, Italy.
34. Kolter JZ, Ng AY. Task-space trajectories via cubic spline optimization, in 2009 IEEE International Conference on Robotics and Automation; 2009; Kobe, Japan.
35. Duburcq A, Chevaleyre Y, Bredeche N, Boéirs G. Online trajectory planning through combined trajectory optimization and function approximation: Application to the Exoskeleton Atalante, in 2020 IEEE International Conference on Robotics and Automation; 2020; Paris, France.
36. Huang JS, Hu PF, Wu KY, Zeng M. Optimal time-jerk trajectory planning for industrial robots. *Mech Mach Theory*. 2018;121:530–544.
37. Zhang SJ, Xing Y, Hu Y. Composite gait optimization method for a multi-legged robot based on optimal energy consumption. *Chi Space Sci Technol*. 2018;38(2):32–39.
38. Mcghee RB, Frank AA. On the stability properties of quadruped creeping gaits. *Math Biosci*. 1968;3(1):331–351.
39. Park H, Kwak B, Bae J. Inverse kinematics analysis and COG trajectory planning algorithms for stable walking of a quadruped robot with redundant DOFs. *J Bionic Eng*. 2018;15(4):610–622.
40. Luat TH, Kim YT. Fuzzy control for walking balance of the biped robot using ZMP criterion. *Int J Hum Robot*. 2017;14(2).
41. Wu DQ, Liu CJ, Zhang JQ, Chen QJ. Survey of locomotion control of legged robots inspired by biological concept. *Sci China Ser F Inf Sci*. 2009;52(10):1715–1729.
42. Qi Y, Li WT, Zhu W. The vehicle-level test of the landing gear system for lunar lander. *Spacecr Environ Eng*. 2020;37(6): 576–581.
43. Yang JZ, Zeng FM, Man JF, Zhu W. Design and verification of the landing impact attenuation system for Chang'E-3 lander. 2014;44(5):440–449.
44. Zhu YG, Jin B. Compliance control of a legged robot based on improved adaptive control: Method and experiments. *Int J Robotics Autom*. 2016;31(5):366–373.
45. Li M, Deng ZQ, Liu RQ, Guo HW. Crashworthiness design optimisation of metal honeycomb energy absorber used in lunar lander. *Int J Crashworth*. 2011;16(4):411–419.